Octupole correlations in collective excitations of neutron-rich N≈56 nuclei

Nomura, Kosuke

Download date / Datum preuzimanja: **2024-11-18**

Repository / Repozitorij:

Repository of the Faculty of Science - University of Zagreb

Octupole correlations in collective excitations of neutron-rich $N \approx 56$ nuclei

Kosuke Nomura [*]

Department of Physics, Faculty of Science, University of Zagreb, HR-10000 Zagreb, Croatia

Octupole correlations in the low-energy collective states of neutron-rich nuclei with the neutron number $N \approx 56$ are studied within the interacting boson model (IBM) that is based on the nuclear density-functional theory. The constrained self-consistent mean-field (SCMF) calculations using a universal energy density functional and a pairing interaction provide the potential-energy surfaces in terms of the axially symmetric quadrupole and octupole deformations for the even-even nuclei $^{86-94}$Se, $^{88-96}$Kr, $^{90-98}$Sr, $^{92-100}$Zr, and $^{94-102}$Mo. The SCMF energy surface is then mapped onto the energy expectation value of a version of the IBM in the boson condensate state, which consists of the neutron and proton monopole s, quadrupole d, and octupole f bosons. This procedure determines the strength parameters of the IBM Hamiltonian, which is used to compute relevant spectroscopic properties. At the SCMF level, no octupole deformed ground state is obtained, while the energy surface is generally soft in the octupole deformation at $N \approx 56$. The predicted negative-parity yrast bands with the bandhead state 3_1^- weakly depend on N and become lowest in energy at $N = 56$ in each of the considered isotopic chains. The model further predicts finite electric octupole transition rates between the lowest negative- and the positive-parity ground-state bands.

I. INTRODUCTION

The ground-state shape and the related spectroscopic properties of those neutron-rich nuclei in the mass $A \approx 100$ region have been of considerable interest. The low-energy structure of these nuclei depends on the underlying shell structures and nuclear forces and is characterized by a subtle interplay between the single-particle and collective degrees of freedom. A number of nuclei belonging to this mass region have been suggested to demonstrate intriguing nuclear shape-related features that include the triaxial deformation, the proton $Z = 40$ and neutron $N = 56$ subshell gaps, the coexistence of several different shapes in the vicinity of the ground state [1], the quantum phase transitions in their shapes [2] represented by a sudden onset of deformation near the neutron number $N \approx 60$.

Of particular interest is the octupole correlations and the related low-energy negative-parity states. In a simple spherical shell model, the octupole correlations become enhanced in particular mass regions in the nuclear mass table, in which the coupling occurs between the normal and unique parity single-particle orbitals in a given major oscillator shell that satisfy the conditions $\Delta \ell = \Delta j = 3\hbar$, with ℓ and j the quantum numbers for a single-particle state. The so-called "octupole magic numbers" at which the above conditions are met and stable octupole deformations are supposed to emerge are the neutron and/or proton numbers 34, 56, 88, 134, ... [3,4]. Experimental evidence for the permanent octupole deformations were found at CERN in the light actinides with $(N, Z) \approx (134, 88)$

such as ^{220}Rn and ^{224}Ra [5], and ^{228}Th [6] and at ANL in the lanthanides with $(N, Z) \approx (88, 56)$ such as ^{144}Ba [7] and ^{146}Ba [8]. On the other hand, the possible octupolarity in the lighter-mass regions, such as those with $(N, Z) \approx (56, 34)$, (56,56), and (34,34), has not been as extensively investigated, both experimentally and theoretically, as in the cases of the actinides and lanthanides.

In some of the neutron-rich even-even Mo, Zr, Sr, and Kr isotopes that are in the vicinity of the neutron number $N \approx 56$, low-lying negative-parity states 3^- at the excitation energy $E_x \approx 2$ MeV, as well as the bands built on them, have been suggested experimentally (see, e.g., Refs. [9–16]). In this case, the negative-parity states are supposed to appear as a consequence of the coupling between the neutron $h_{11/2}$ and $d_{5/2}$ orbitals. In the neutron-rich nuclei ^{94,96}Kr, in particular, the 3^- states have been newly obtained in an experiment at RIKEN [16]. With the recurrent interests in the studies of the octupole shapes and the new data on the negative-parity states in radioactive nuclei, it would be meaningful to pursue timely theoretical investigations to address the relevance of the octupole degrees of freedom in the description of low-lying nuclear structure in the neutron-rich $A \approx 100$ region.

Theoretical approaches to the octupole deformations and collective excitations include the self-consistent mean-field (SCMF) framework based on the macroscopic-microscopic method with Strutinski shell correction [17–19] and the energy density functionals (EDFs) [20–37], the interacting boson model (IBM) [38–56], the geometrical collective model [57–60], the cluster models [61–63], and the nuclear shell model [64–67]. In particular, the SCMF methods using a given universal nonrelativistic [34,68] or relativistic [69,70]

---
*knomura@phy.hr

EDF provides a global description of the bulk nuclear matter and intrinsic properties, as well as collective excitations, over the entire region of the nuclear mass table. In recent years, the EDF-based approaches have been extensively used for the studies of the octupole deformations and collectivity. A straightforward approach is the beyond-SCMF calculations with symmetry projections and configuration mixing within the generator coordinate method (GCM) [20–25,27–29,33,34,36,71]. The full GCM calculations are, however, computationally so demanding that some alternative approaches have also been considered, such as the mapping onto the quadrupole-octupole collective Hamiltonian [26,30,37] and onto the interacting-boson Hamiltonian [48–50].

In this article, the octupole correlations and the relevant spectroscopic properties of the low-lying positive- and negative-parity states in the neutron-rich nuclei near the octupole magic number $N = 56$ are investigated within the framework of the nuclear EDF and the mapped IBM. The starting point is the axially symmetric quadrupole and octupole constrained SCMF calculations of the potential-energy surfaces for those nuclei in which octupolarity is expected to be enhanced, i.e., $^{86-94}$Se, $^{88-96}$Kr, $^{90-98}$Sr, $^{92-100}$Zr, and $^{94-102}$Mo. Then, by using the method of Ref. [49], the quadrupole-octupole SCMF energy surface is mapped onto the equivalent one in the system of the interacting monopole s, quadrupole d, and octupole f bosons. The mapping procedure specifies the strength parameters for the sdf-IBM Hamiltonian, which in turn gives excitation spectra and electromagnetic transition rates of both the positive- and negative-parity states. Previously, the mapped sdf-IBM framework has been applied to the studies of octupole shape phase transitions in light actinides and rare-earth nuclei using the relativistic EDF [48,49]. A number of spectroscopic calculations have been carried out based on the Gogny-type EDF [34], and revealed the onset of octupole deformations and collectivity in various mass regions characteristic of the octupole deformations [50–54].

In the present study, a version of the sdf-IBM that makes distinction between the neutron and proton boson degrees of freedom, denoted hereafter by sdf-IBM-2, is considered since it is more realistic than a simpler version of the IBM (sdf-, or $spdf$-IBM-1) that does not distinguish between the protons and neutrons. In most of the previous IBM calculations for the octupole collective states, the simple IBM-1 framework has been employed. There are a few instances in which the sdf-IBM-2 has been considered on phenomenological grounds, e.g., in Refs. [44,46,47,56]. In this study, all the strength parameters for the sdf-IBM-2 are determined by using the microscopic input from the constrained SCMF calculations. As a basis of the SCMF method, the relativistic density-dependent point-coupling (DD-PC1) EDF [72] is employed. The universal functional DD-PC1 has been successfully employed in the spectroscopic studies on the octupole collective modes both at the static and beyond SCMF levels [31,33,37].

The paper is structured as follows. In Sec. II the theoretical procedure in the mapped sdf-IBM-2 calculations is illustrated. Results of the quadrupole-octupole constrained potential-energy surfaces, the systematics of the low-energy spectra for the positive- and negative-parity states, electric

quadrupole, octupole, and dipole transition rates that characterize the octupole correlations in the considered Se, Kr, Sr, Zr, and Mo nuclei are discussed in Sec. III. In the same section detailed level structures for the octupole magic nuclei, i.e., the $N = 56$ isotones, are analyzed, with a special attention to the neutron-rich Kr isotopes, where some new experimental data are available. Finally, Sec. IV gives a summary of the main results and conclusions.

II. THEORETICAL FRAMEWORK

A. Self-consistent mean-field calculations

The constrained SCMF calculations are performed within the relativistic Hartree-Bogoliubov (RHB) framework [69,70,73] using the DD-PC1 interaction for the particle-hole channel and a separable pairing force of finite range [74] for the particle-particle channel. The constraints imposed in the SCMF calculations are on the expectation values of the axially symmetric quadrupole $\hat{Q}_{20}$ and octupole $\hat{Q}_{30}$ moments,

$$\hat{Q}_{20} = 2z^2 - x^2 - y^2, \tag{1}$$

$$\hat{Q}_{30} = 2z^3 - 3z(x^2 + y^2), \tag{2}$$

which are associated with the dimensionless quadrupole β_2 and octupole β_3 deformations through the relations

$$\beta_2 = \frac{\sqrt{5\pi}}{3r_0^2 A^{5/3}} \langle \hat{Q}_{20} \rangle, \tag{3}$$

$$\beta_3 = \frac{\sqrt{7\pi}}{3r_0^3 A^2} \langle \hat{Q}_{30} \rangle, \tag{4}$$

with $r_0 = 1.2$ fm. The RHB equation is solved in a harmonic-oscillator basis with the number of oscillator shells $N_F = 12$. Here the strength of the pairing force $V_0 = 837$ MeV fm^3, corresponding to an increase of the original value 728 MeV fm^3 of Ref. [74] by 15%, is used for both the proton and neutron pairs. An effect of increasing the pairing strength in the SCMF calculations is such that the potential-energy surface becomes less steep. The mapping procedure then provides the IBM parameters closer to those that would be obtained in the conventional IBM fit and is expected to give a better description of the experimental excitation energies, especially, those for nonyrast states. As a further support for the enhancement of the pairing strength, a global analysis of the separable pairing force over the entire region of the mass chart based on the covariant density-functional theory [75] indicated that, in order to account for the empirical odd-even mass staggering, the strength of the pairing force needs to be scaled with nucleon-number-dependent factors. In the case of the $N \approx 56$ nuclei considered here, such scaling factors are calculated to be approximately within the range 1.1–1.2, which is consistent with the 15% increase of the pairing strength in the present study. The constrained calculations provide the potential-energy surfaces $E(\beta_2, \beta_3)$ as functions of the β_2 and β_3 deformations. The corresponding results are shown in Figs. 1 and 2, and will be discussed in detail in Sec. III A. The β_2-β_3 energy surface has a property that it is symmetric with respect to the $\beta_3 = 0$ axis, i.e., $E(\beta_2, \beta_3) = E(\beta_2, -\beta_3)$, and it is therefore enough to consider the $\beta_3 \geqslant 0$ sector of the energy surface.
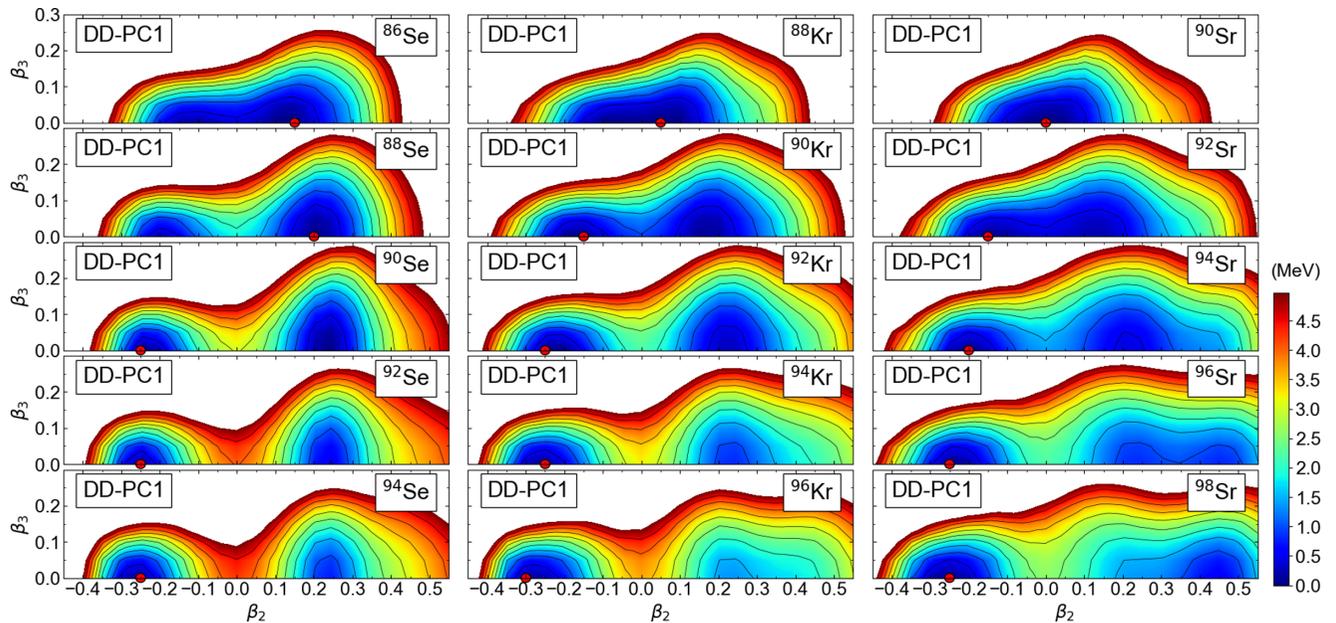
FIG. 1. Axially symmetric quadrupole and octupole SCMF potential-energy surfaces for the $^{86-94}$Se, $^{88-96}$Kr, and $^{90-98}$Sr isotopes as functions of the β_2 and β_3 deformations, computed by the constrained RHB method with the DD-PC1 EDF and the separable pairing force of finite range. The energy difference between neighboring contours is 0.5 MeV, and the global minimum within the β_2-β_3 plane is indicated by the solid circle.

B. Mapping onto the *sdf*-IBM-2 Hamiltonian

The *sdf*-IBM-2 is comprised of the neutron and proton monopole s_ν and s_π, quadrupole d_ν and d_π, and octupole f_ν and f_π bosons, which are, from a microscopic point of view [76,77], associated with the correlated pairs of valence neutrons and protons with spin and parity $J = 0^+$, 2^+, and

3^-, respectively. The calculations are carried out within the neutron $N = 50$–82 and proton $Z = 28$–50 major shells and, therefore, the doubly magic nucleus ^{78}Ni is taken as the inert core. The number of the neutron (or proton) bosons n_ν (or n_π) is conserved for each nucleus, and is equal to half the number of valence neutron (or proton) pairs. The neutron (or
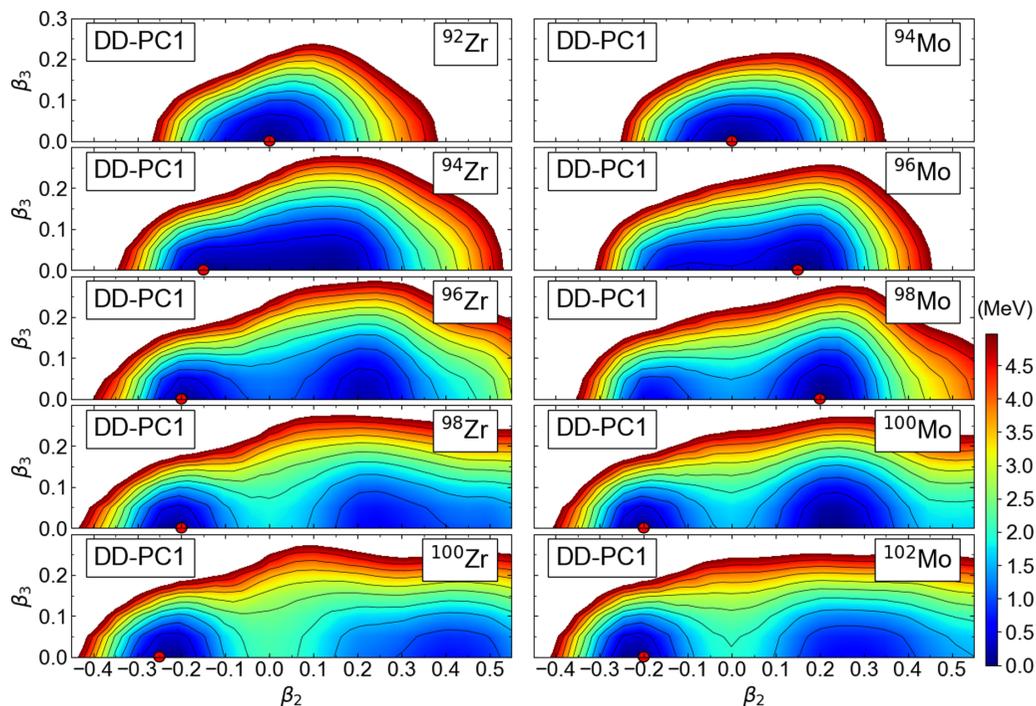
FIG. 2. Same as Fig. 1, but for the $^{92-100}$Zr, and $^{94-102}$Mo isotopes.

proton) s_ν (s_π), d_ν (d_π), and f_ν (f_π) bosons, denoted n_{s_ν}, n_{d_ν}, and n_{f_ν} (n_{s_π}, n_{d_π}, and n_{f_π}), respectively, satisfy the condition that $n_{s_\nu} + n_{d_\nu} + n_{f_\nu} = n_\nu$ (or $n_{s_\pi} + n_{d_\pi} + n_{f_\pi} = n_\pi$).

Based on the earlier microscopic considerations [76] that the low-lying structure of medium-heavy and heavy nuclei is mainly determined by the pairing-like correlations between identical nucleons and the quadrupole-quadrupole interactions between nonidentical nucleons, the following form of the sdf-IBM-2 Hamiltonian is adopted:

$$\hat{H} = \epsilon_d \hat{n}_d + \epsilon_f \hat{n}_f + \kappa_2 \hat{Q}_\nu \cdot \hat{Q}_\pi + \kappa_3 \hat{O}_\nu \cdot \hat{O}_\pi. \quad (5)$$

The first (second) term stands for the d (f) boson number operator $\hat{n}_d = \hat{n}_{d_\nu} + \hat{n}_{d_\pi}$ ($\hat{n}_f = \hat{n}_{f_\nu} + \hat{n}_{f_\pi}$) with the single d (f) boson energy ϵ_d (ϵ_f) relative to the s-boson one. The single boson energies, ϵ_d and ϵ_f, could in principle be different, but are here assumed to be the same for simplicity, between the neutron and proton bosons. The third term is the quadrupole-quadrupole interaction with the strength κ_2, with the quadrupole operator given by

$$\hat{Q}_\rho = s_\rho^\dagger \tilde{d}_\rho + d_\rho^\dagger s_\rho + \chi_\rho (d_\rho^\dagger \times \tilde{d}_\rho)^{(2)} + \chi_\rho'(f_\rho^\dagger \times \tilde{f}_\rho)^{(2)} \quad (6)$$

for neutron $\rho = \nu$ and proton $\rho = \pi$. χ_ρ and χ_ρ' are dimensionless parameters. The last term in (5) represents the octupole-octupole interaction between the neutron and proton bosons with the strength κ_3 and the octupole operator is given as

$$\hat{O}_\rho = s_\rho^\dagger \tilde{f}_\rho + f_\rho^\dagger s_\rho + \chi_\rho''(d_\rho^\dagger \times \tilde{f}_\rho + f_\rho^\dagger \times \tilde{d}_\rho)^{(3)}, \quad (7)$$

with another dimensionless parameter χ_ρ''.

To make a connection between the geometrical structure of a multifermion systems specified by the β_2 and β_3 deformations and the boson Hamiltonian (5), the following wave function for the condensate state [78] of the s_ν, s_π, d_ν, d_π, f_ν, and f_π bosons is considered:

$$|\Psi\rangle = \prod_{\rho=\nu,\pi} \frac{1}{\sqrt{n_\rho!}} (\lambda_\rho^\dagger)^{n_\rho} |0\rangle, \quad (8)$$

with

$$\lambda_\rho^\dagger = s_\rho^\dagger + \tilde{\beta}_{2\rho} d_{\rho,0}^\dagger + \tilde{\beta}_{3\rho} f_{\rho,0}^\dagger, \quad (9)$$

and $|0\rangle$ the boson vacuum, i.e., the inert core. The amplitudes $\tilde{\beta}_{2\rho}$ and $\tilde{\beta}_{3\rho}$ in (9) are boson analogs of the quadrupole β_2 and octupole β_3 deformations, respectively. The expectation value of the sdf-IBM-2 Hamiltonian gives energy surface of the boson system specified by the four variables $\tilde{\beta}_{2\nu}$, $\tilde{\beta}_{2\pi}$, $\tilde{\beta}_{3\nu}$, and $\tilde{\beta}_{3\pi}$. However, to treat the energy surface in the full four-dimensional space is practically so complicated that, in this study, it is assumed that the neutron and proton bosons should have the same deformations, i.e., $\tilde{\beta}_{2\nu} = \tilde{\beta}_{2\pi} \equiv \tilde{\beta}_2$ and $\tilde{\beta}_{3\nu} = \tilde{\beta}_{3\pi} \equiv \tilde{\beta}_3$. The equal deformations for the neutron and proton bosons may seem practically equivalent to the mapping onto the sdf-IBM-1 system. An advantage of using the sdf-IBM-2 is that it produces more eigenstates than the sdf-IBM-1, for the latter represents the fully symmetric states of the former. Therefore, the sdf-IBM-2 is expected to give a better description of the spectroscopic properties of the low-lying states, especially the $M1$ transitions, than in the sdf-IBM-1. Under the assumption of the equal proton and

neutron deformations, the bosonic potential-energy surface in the $\tilde{\beta}_2$-$\tilde{\beta}_3$ space is calculated as

$$
\begin{aligned}
&\frac{\langle\Psi|\hat{H}|\Psi\rangle}{\langle\Psi|\Psi\rangle} \\
&= \frac{(n_\nu + n_\pi)(\epsilon_d \tilde{\beta}_2^2 + \epsilon_f \tilde{\beta}_3^2)}{1 + \tilde{\beta}_2^2 + \tilde{\beta}_3^2} + \frac{n_\nu n_\pi}{(1 + \tilde{\beta}_2^2 + \tilde{\beta}_3^2)^2} \\
&\times \Bigg[\kappa_2\left(2\tilde{\beta}_2 - \sqrt{\frac{2}{7}}\chi_\nu\tilde{\beta}_2^2 - \frac{2}{\sqrt{21}}\chi_\nu'\tilde{\beta}_3^2\right) \\
&\times \left(2\tilde{\beta}_2 - \sqrt{\frac{2}{7}}\chi_\pi\tilde{\beta}_2^2 - \frac{2}{\sqrt{21}}\chi_\pi'\tilde{\beta}_3^2\right) \\
&+ \kappa_3\left(2\tilde{\beta}_3 - \frac{4}{\sqrt{15}}\chi_\nu''\tilde{\beta}_2\tilde{\beta}_3\right)\left(2\tilde{\beta}_3 - \frac{4}{\sqrt{15}}\chi_\pi''\tilde{\beta}_2\tilde{\beta}_3\right)\Bigg].
\end{aligned}
$$
$$(10)$$

The strength parameters of the boson Hamiltonian (5) to be determined are $\{\epsilon_d, \epsilon_f, \kappa_2, \chi_\nu, \chi_\pi, \chi_\nu', \chi_\pi', \kappa_3, \chi_\nu'', \chi_\pi''\}$. To reduce the number of parameters, it is assumed that the dimensionless parameters $\chi_\nu', \chi_\pi', \chi_\nu''$, and χ_π'' are all equal, $\chi_\nu' = \chi_\pi' = \chi_\nu'' = \chi_\pi'' \equiv \chi$. It is further assumed that the bosonic deformation $\tilde{\beta}_\lambda$ ($\lambda = 2$ or 3) is proportional to the fermionic counterparts, i.e., $\tilde{\beta} \equiv C_\lambda \beta_\lambda$. C_λ is a constant of proportionality, and is also determined by the procedure described below.

The seven parameters for the sdf-IBM-2 Hamiltonian, i.e., $\{\epsilon_d, \epsilon_f, \kappa_2, \chi_\nu, \chi_\pi, \kappa_3, \chi\}$ and the two constants C_2 and C_3, are determined for each nucleus by mapping the axially symmetric β_2-β_3 SCMF potential-energy surface onto the corresponding bosonic energy surface given by Eq. (10). Or equivalently, these strength parameters are fine tuned so that the sdf-IBM-2 energy surface of (10) becomes similar in topology to the SCMF one and that the approximate equality

$$E_{\text{SCMF}}(\beta_2, \beta_3) \approx E_{\text{IBM}}(\beta_2, \beta_3) \quad (11)$$

should be satisfied in the neighborhood of the global minimum. Limiting the range within which the mapping of (11) is to be made to the vicinity of the global mean-field minimum is due to the fact that in the SCMF framework, the configurations near the global minimum make the most relevant contributions to determining the low-energy collective states. On the other hand, the regions very far from the minimum with large β_2 and β_3 deformations are more dominated by the quasiparticle degrees of freedom, which are, by construction, not taken into account in the present sdf-IBM-2 framework. For further details of the mapping procedure, the reader is referred to Refs. [48,49,79,80].

Diagonalization of the mapped sdf-IBM-2 Hamiltonian with the strength parameters determined by the aforementioned procedure produces excitation spectra for both parities and electromagnetic transition rates. For the numerical diagonalization of the Hamiltonian, the computer program ARBMODEL [81] is used.
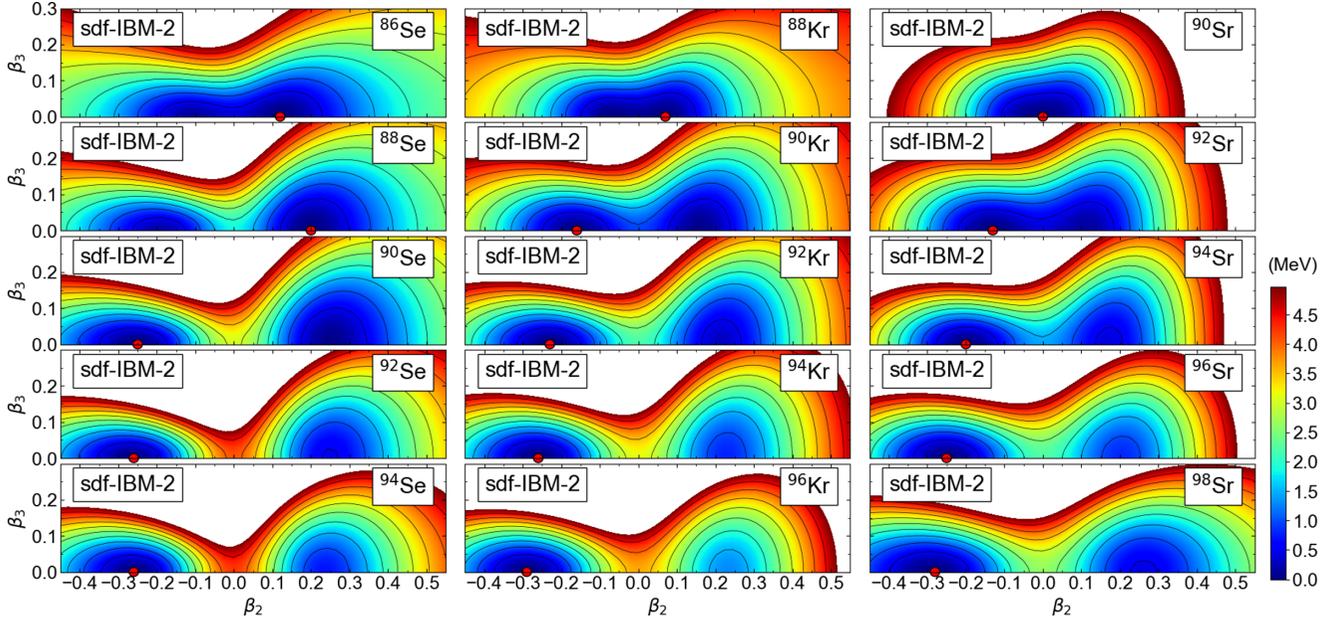
FIG. 3. Same as Fig. 1, but for the mapped sdf-IBM-2 potential-energy surfaces for the $^{86-94}$Se, $^{88-96}$Kr, and $^{90-98}$Sr isotopes.

III. RESULTS AND DISCUSSION

A. Potential-energy surfaces

Figures 1 and 2 show contour plots of the axially symmetric quadrupole and octupole deformation-energy surfaces for the even-even nuclei $^{86-94}$Se, $^{88-96}$Kr, $^{90-98}$Sr, $^{92-100}$Zr, and $^{94-102}$Mo as functions of the β_2 and β_3 deformations, computed by the SCMF method described in Sec. II A. For any of the nuclei under study, one finds no octupole deformed ground-state minimum with $\beta_3 \neq 0$. On closer inspection, the potential-energy surface appears to be most rigid in the β_2 deformation at the $N = 56$ nucleus among each isotopic chain, the neutron number corresponding to the empirical octupole magic number. The potential only gradually becomes softer along the β_3 direction from $N = 52$ to 56. The β_3-softest potential is obtained for those nuclei with the neutron number approximately equal to 54 or 56, for which nuclei the curvature of the energy surface at the global minimum on the $\beta_3 = 0$ axis is indeed smallest. These features are most notably observed in the Se and Kr isotopes, with the proton number of the former isotopes, $Z = 34$, identified as the proton octupole magic number. For the $N > 56$ nuclei, the energy surfaces become more rigid, especially in the β_3 deformation, and the octupole correlations are expected to be much less pronounced.

There are some other properties worth remarking of the SCMF energy surfaces. For the $N = 52$ isotones, a nearly spherical minimum is suggested: $\beta_2 \approx 0.05$ for ^{86}Se and ^{88}Kr, and $\beta_2 \approx 0.0$ for ^{90}Sr, ^{92}Zr, and ^{94}Mo, the last three nuclei being in the immediate vicinity of the proton subshell closure $Z = 40$. All the $N = 54$ isotones are here suggested to be soft in β_2 deformation in the interval $|\beta_2| \lesssim 0.2$. In all the isotopic chains, the prolate-to-oblate shape transition is observed: in Figs. 1 and 2 a change in the location of the minimum from the prolate, or nearly spherical, to oblate sides at $N = 54$ (Kr

and Zr), $N = 56$ (Se), and $N = 58$ (Mo). In ^{96,98}Sr and ^{100}Zr, another prolate minimum with quite a large β_2 deformation ($\beta_2 \gtrsim 0.4$) appears. These behaviors are considered a signature of the onset of intruder deformed configuration that is suggested to occur around $N = 60$.

It can be also shown that the SCMF calculations with the reduced pairing strength $V_0 = 728$ MeV fm^3 produce the energy surfaces that are slightly steeper in both β_2 and β_3 deformations but that are qualitatively similar to those shown in Figs. 1 and 2, obtained with the increased pairing strength $V_0 = 837$ MeV fm^3. In addition, the same constrained RHB calculations, but employing the density-dependent meson-exchange (DD-ME2) functional [82], another representative effective interaction in the relativistic EDF framework, give strikingly similar mean-field results to those in the case of the DD-PC1 EDF.

Figures 3 and 4 show the mapped sdf-IBM-2 potential-energy surfaces. As compared with the SCMF energy surfaces in Figs. 1 and 2, one notices that the basic topology of the SCMF energy surface, up to typically 2 MeV excitation from the minimum, is reproduced by the bosonic ones. One also finds that the sdf-IBM-2 energy surfaces are flat for higher excitation energies associated with large β_2 and β_3 deformations, in comparison to the SCMF counterparts. This difference illustrates that the sdf-IBM-2 space consists of only limited number of valence nucleons, while the SCMF model includes all nucleon degrees of freedom.

B. Derived strength parameters

The derived sdf-IBM-2 strength parameters used for the spectroscopic calculations on the considered Se, Kr, Sr, Zr, and Mo nuclei are shown as functions of N in Fig. 5. In Fig. 5(a) one sees that the single-d boson energy ϵ_d is mostly stable for $52 \lesssim N \lesssim 58$, but gradually decreases along the
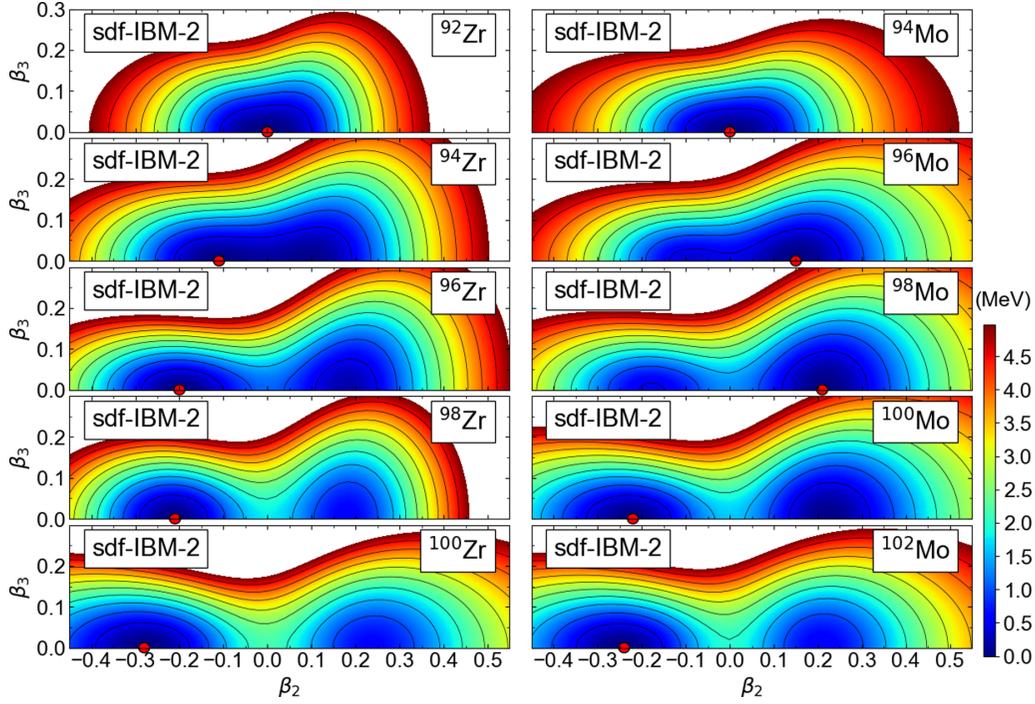
FIG. 4. Same as Fig. 3, but for the $^{92-100}$Zr, and $^{94-102}$Mo isotopes.

Mo chain. A sudden drop from $N = 58$ to 60 in the derived ϵ_d for the Sr and Zr isotopes is partly to account for the rapid structural change, i.e., onset of strong deformation, suggested empirically in these isotopic chains. The quadrupole-quadrupole interaction strength κ_2 generally decreases in magnitude as the number of valence neutrons increases [cf. Fig. 5(b)]. The parameters χ_ν [Fig. 5(c)] and χ_π [Fig. 5(d)] do not show any strong dependence on N, except for the χ_ν value for the Mo isotopes. The positive (negative) sign of the sum $\chi_\nu + \chi_\pi$ determines whether a nucleus is oblate (prolate) deformed. In many of the considered nuclei, a weakly deformed mean-field minimum occurs on the oblate side, hence the value of the sum $\chi_\nu + \chi_\pi$ here has positive sign and small magnitude. The single f-boson energy ϵ_f is here basically kept constant or made only gradually change within the range $\epsilon_f \simeq 2.7$–3.0 MeV, while it significantly decreases with N for the Mo isotopic chain [Fig. 5(e)]. The value of the common parameter $\chi(= \chi_\nu' = \chi_\pi' = \chi_\nu'' = \chi_\pi'')$ in Fig. 5(f) is determined according to the degree of the β_3, as well as β_2, softness of the potential. One sees that the derived χ value is indeed large in magnitude for $52 \lesssim N \lesssim 56$ as compared with those nuclei with $N > 56$ for most of the studied isotopic chains. A fixed value of the octupole-octupole interaction strength $\kappa_3 = 0.12$ MeV, determined for a particular nucleus ^{92}Kr, is here used for all the nuclei under study. The use of the constant κ_3 value is not only for the sake of simplicity to reduce the number of parameters, but is also to take into account the facts that the topology of the SCMF energy surface varies only gradually in the β_3 deformation as a function of the nucleon number, and that the observed low-lying negative-parity levels also do not show a strong nucleon-number dependence.

C. Systematics of low-energy spectra

Figure 6 compares the calculated low-energy spectra for the positive-parity even-spin states 2_1^+, 4_1^+, and 6_1^+ of the considered nuclei with the experimental data [83]. One observes an overall reasonable agreement with the data, except perhaps for the Zr isotopes. For the Se, Kr, and Mo isotopes, both the theoretical and experimental energy levels are gradually lowered with the increasing N. The modest decrease of the calculated yrast spectra, from ^{94}Kr to ^{96}Kr in particular, suggests a smooth onset of deformation in agreement with the experiment [88]. For the Sr and Zr isotopic chains the present calculation gives a more rapid decrease of these states. One notices, in the corresponding experimental spectra in Figs. 6(c) and 6(d), a pronounced peak at the neutron number $N = 56$. This indicates the effect of the neutron $N = 56$ subshell gap due to the filling in the $\nu d_{5/2}$ orbital, which is even more enhanced for the Zr nuclei corresponding to the proton subshell closure $Z = 40$. The mapped sdf-IBM-2 does not reproduce this trend in Zr, mainly because no spherical minimum occurs in the axially symmetric quadrupole-octupole SCMF energy surface for ^{96}Zr (cf. Fig. 2). The SCMF calculation gives for this nucleus only a weakly deformed oblate minimum at $\beta_2 \approx -0.2$, and consequently the mapped sdf-IBM-2 yields the collective energy spectrum, characterized by the low-lying 2_1^+ energy level and by the ratio of the 4_1^+ to 2_1^+ excitation energies $R_{4/2} = 2.46$. Another notable feature observed in the Sr and Zr isotopes is a sudden drop of the energy levels from $N = 58$ to 60. The present calculation reproduces well this systematic. As for the $N = 52$ isotones, the sdf-IBM-2 generally does not give a very good description because these nuclei are close to the neutron $N = 50$ major shell closure and the model space of the calculation including
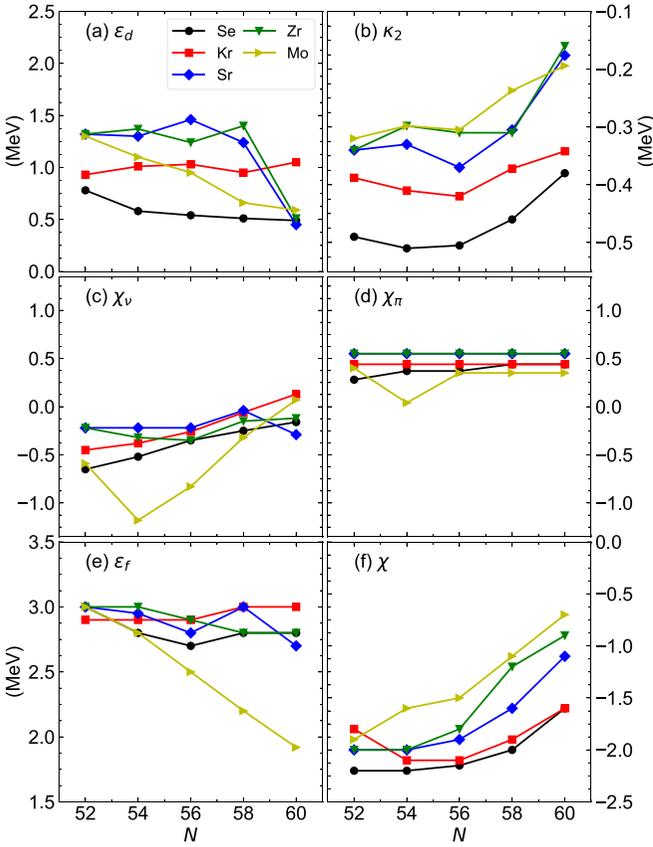
FIG. 5. Values of the strength parameters for the sdf-IBM-2 Hamiltonian, plotted as functions of N. Note that the parameter χ in panel (f) is defined as $\chi = \chi'_\nu = \chi'_\pi = \chi''_\nu = \chi''_\pi$. The octupole-octupole interaction strength κ_3 is kept constant as $\kappa_3 = 0.12$ MeV and is not plotted.

only one neutron boson may not be large enough to reproduce the positive-parity levels of the nearly spherical nuclei. It is worth noting that the low-lying nuclear structure in the $N \approx 60$ region is often characterized by the occurrence of the competing intrinsic shapes, and that a more refined calculation of the relevant spectroscopic properties would need to include the configuration mixing between the normal and intruder states [89] within the sdf-IBM.

In Fig. 7, the calculated energy spectra for the low-lying negative-parity odd-spin states 1^-_1, 3^-_1, 5^-_1, and 7^-_1 are shown as functions of N. Of particular interest regarding the predicted negative-parity energy spectra is their parabolic dependence with N with the minimum values at $N = 56$ for all the considered isotopic chains, except for Mo. This result is consistent with the systematic behavior of the quadrupole-octupole potential-energy surfaces, which exhibit the β_3 softest potential for those nuclei with $N \approx 56$. As seen in Fig. 7, in accordance with the experimental data, the lowest negative-parity state is here predicted to be $I = 3^-$ at the excitation energy $E_x \approx 2$ MeV. Within the calculation, the 1^- energy level is rather high and is close to the 5^-_1 one. This level structure is at variance with those observed, e.g., in the actinide nuclei with $N \approx 134$. In many of the nuclei in the latter mass region, the low-lying negative-parity band

with the bandhead 1^- state appears and forms an approximate alternating-parity rotational band with the positive-parity ground-state band. One may notice that the predicted higher-spin negative-parity states, especially the 7^-_1 one, is higher than the experimental value, most notably, for ^{94,96}Se and ^{94}Kr. It is noted, however, that the observed low-lying 7^- state in these nuclei could be attributed to isomeric state based on the neutron two-quasiparticle excitations (see, e.g., Ref. [87]), which are beyond the present sdf-IBM-2 model space.

D. f-boson contributions to wave functions

To interpret the nature of the low-lying states, contributions of the f bosons to the corresponding sdf-IBM-2 wave functions are studied. As an illustrative example, Fig. 8 shows the expectation values of the neutron $\hat{n}_{f_\nu}$ and proton $\hat{n}_{f_\pi}$ boson number operators calculated by using the wave functions for the low-spin positive-parity states 0^+_1, 2^+_1, 0^+_2, and 2^+_2, and negative-parity states 1^-_1, and 3^-_1. As one can see in Figs. 8(a) to 8(d) and 8(g) to 8(j), there is only a small admixture of the f_ν and f_π bosons into the low-energy positive-parity states, with the expectation value $\hat{n}_{f_\rho}$ typically $\langle \hat{n}_{f_\rho} \rangle \lesssim 0.2$. In the 0^+_2 wave functions there appears to be a relatively large f-boson contributions at $N = 56$, in particular, for ^{90}Se, ^{92}Kr, and ^{94}Sr, in which nuclei the octupole correlations are expected to be most pronounced. For the negative-parity states 1^-_1 and 3^-_1, the calculated expectation value $\langle \hat{n}_{f_\rho} \rangle \approx 0.5$ for both proton and neutron bosons, and hence $\langle \hat{n}_{f_\rho} + \hat{n}_{f_\rho} \rangle \approx 1$. Therefore, the wave functions for the above negative-parity states contain approximately one-f boson components.

E. Electromagnetic transition properties

Electromagnetic properties considered in the present theoretical analysis are those of the electric-quadrupole $E2$, octupole $E3$, dipole $E1$, and magnetic-dipole $M1$ transitions. The corresponding operators read

$$\hat{T}^{(E2)} = \sum_{\rho = \nu, \pi} e_{2,\rho} \hat{Q}_\rho, \tag{12}$$

$$\hat{T}^{(E3)} = \sum_{\rho = \nu, \pi} e_{3,\rho} \hat{O}_\rho, \tag{13}$$

$$\hat{T}^{(E1)} = \sum_{\rho = \nu, \pi} e_{1,\rho} \hat{D}_\rho, \tag{14}$$

$$\hat{T}^{(M1)} = \sqrt{\frac{3}{4\pi}} \sum_{\rho = \nu, \pi} g_\rho \hat{L}_\rho, \tag{15}$$

where the operators $\hat{Q}_\rho$ and $\hat{O}_\rho$ are the same quadrupole and octupole operators as in the Hamiltonian (5) with the same values of the parameters χ_ρ, χ'_ρ, and χ''_ρ, and

$$\hat{D}_\rho = (d^\dagger_\rho \times \tilde{f}_\rho + f^\dagger_\rho \times \tilde{d}_\rho)^{(1)}, \tag{16}$$

$$\hat{L}_\rho = \sqrt{10}(d^\dagger_\rho \times \tilde{d}_\rho)^{(1)} + \sqrt{28}(f^\dagger_\rho \times \tilde{f}_\rho)^{(1)} \tag{17}$$

are electric- and magnetic-dipole transition operators, respectively. $e_{\lambda,\rho}$ ($\lambda = 1, 2, 3$) in Eqs. (12)–(14) are effective boson charges, and g_ρ in (15) is the bosonic gyromagnetic (g) factor. The neutron and proton effective charges are assumed to
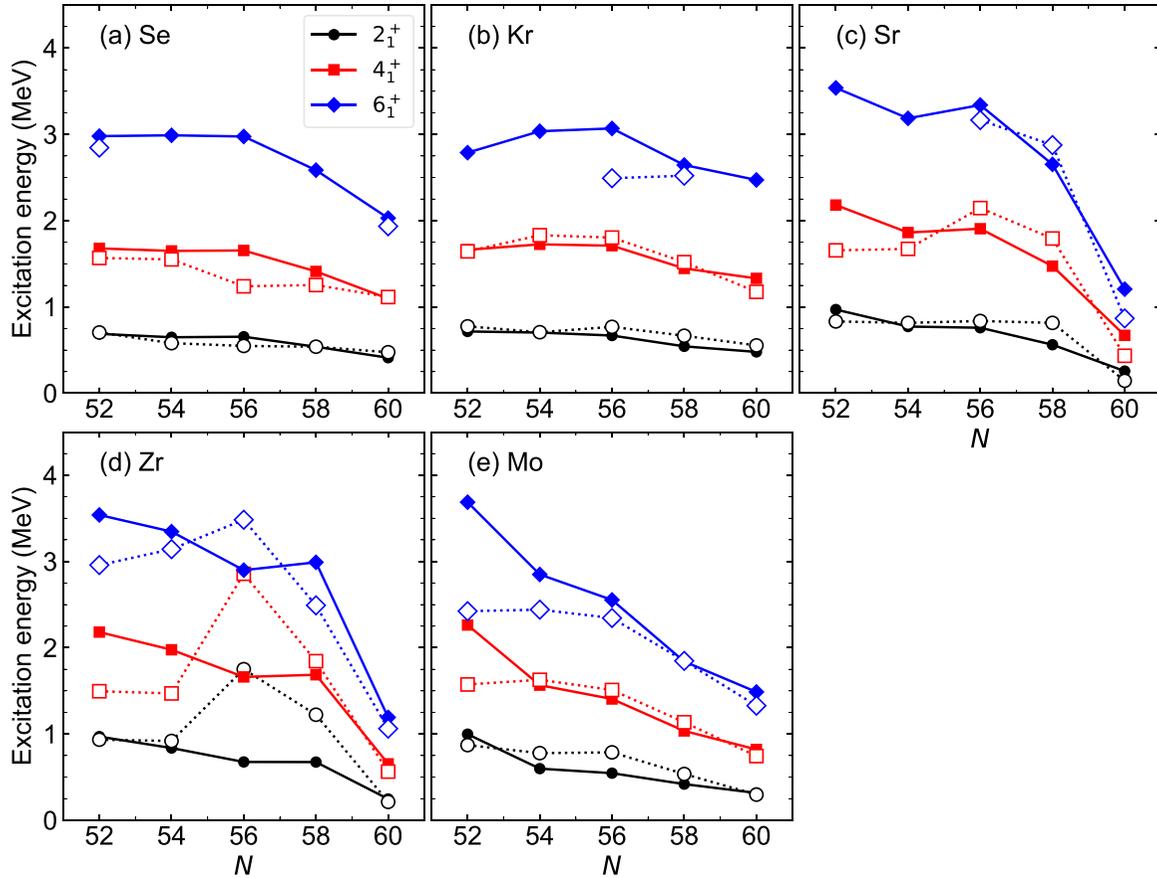
FIG. 6. Low-energy spectra for positive-parity even-spin states 2_1^+, 4_1^+, and 6_1^+ of the considered even-even nuclei $^{86-94}$Se, $^{88-96}$Kr, $^{90-98}$Sr, $^{92-100}$Zr, and $^{94-102}$Mo. Theoretical and experimental values are represented by the solid and open symbols, which are connected by the solid and dotted lines, respectively. The experimental data are taken from Refs. [9,10,16,83–87].

be equal, i.e., $e_{1,\nu} = e_{1,\pi} \equiv e_1$, $e_{2,\nu} = e_{2,\pi} \equiv e_2$, and $e_{3,\nu} = e_{3,\pi} \equiv e_3$, and the fixed effective charges $e_1 = 0.005 \, e\,\mathrm{b}^{1/2}$, $e_2 = 0.06 \, e\,\mathrm{b}$, and $e_3 = 0.06 \, e\,\mathrm{b}^{3/2}$ are used so as to reasonably reproduce the experimental data. The empirical boson g factors $g_\nu = 0\mu_N$ and $g_\pi = 1\mu_N$ are adopted by following the microscopic calculations in the previous (sd-)IBM-2 studies [94].

Systematic behaviors of the reduced $E2$, $E3$, and $E1$ transition probabilities between the lowest positive- and negative-parity states, $B(E2; 2_1^+ \to 0_1^+)$, $B(E3; 3_1^- \to 0_1^+)$, and $B(E1; 3_1^- \to 2_1^+)$, are shown in Fig. 9. Results for the $M1$ properties are discussed in the next section for individual nuclei. Both the calculated and experimental $2_1^+ \to 0_1^+ E2$ transition rates are weak for $52 \leqslant N \leqslant 58$, with the $B(E2)$ values typically lower than 20 Weisskopf units (W.u.). The experimental data show a significant rise of the $B(E2; 2_1^+ \to 0_1^+)$ values from $N = 58$ to 60 in the Sr, Zr, and Mo isotopes, as a consequence of the onset of strong quadrupole deformation. The current model calculation is not able to reproduce this sharp increase of the $B(E2; 2_1^+ \to 0_1^+)$ values. The inconsistency could have arisen mainly due to the fact that the present IBM framework does not include the configuration mixing, which would be required for dealing with the phenomenon of shape coexistence. Indeed, the SCMF potential-energy sur-

face, e.g., for ^{98}Sr, indicates a development of a strongly deformed prolate local minimum at $\beta_2 \approx 0.45$ in addition to the oblate global minimum at $\beta_2 \approx -0.25$ (see Fig. 1). For the Zr and Mo isotopes, on the other hand, the SCMF β_2-β_3 energy surface shown in Fig. 2 does not exhibit a substantial variation from $N = 58$ to 60 along the β_2 deformation, or a pronounced competition between different mean-field minima. It is, therefore, not straightforward to uniquely identify the major source of the discrepancy between the predicted and experimental $B(E2)$ systematics in the Zr and Mo chains. It could be attributed to the lack of the configuration mixing in the IBM, but may also indicate a deficiency of the employed EDF or particular choice of the pairing strength. In addition, only the axially symmetric shape degrees of freedom are considered here as relevant collective coordinates, while the triaxial deformation could also play an important role in the considered mass region.

The $B(E3; 3_1^- \to 0_1^+)$ rates are a direct measure of the octupole collectivity, and are generally large for those nuclei that are expected to have an enhanced octupole deformation. Experimental data for the $B(E3; 3_1^- \to 0_1^+)$ rates are available [13,15,90] for Zr and Mo nuclei. One finds in Fig. 9(d) that experimental $B(E3; 3_1^- \to 0_1^+)$ value is particularly large for ^{96}Zr, 57 ± 4 W.u., and slowly increases toward the middle of
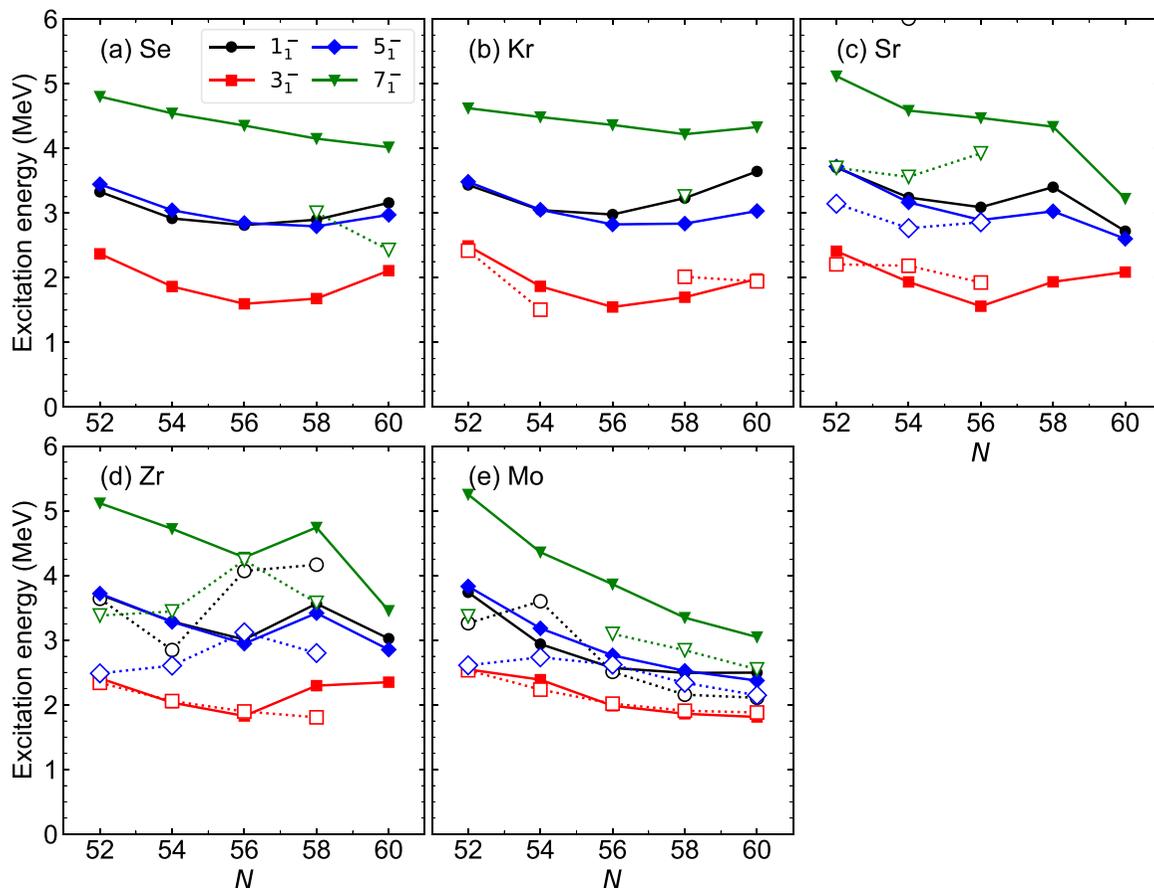
FIG. 7. Same as Fig. 6, but for negative-parity odd-spin states 1_1^-, 3_1^-, 5_1^-, and 7_1^-.
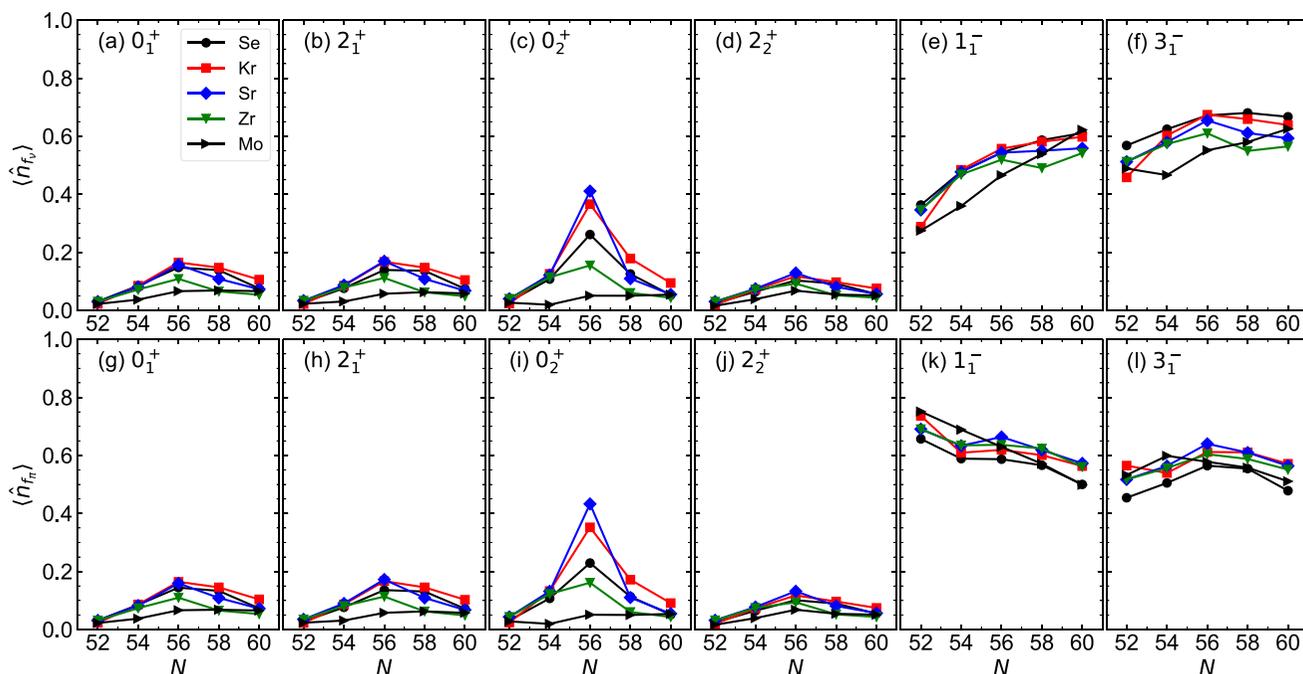
FIG. 8. Expectation values of neutron $\hat{n}_{f_\nu}$ (upper row) and proton $\hat{n}_{f_\pi}$ (lower row) number operators calculated for the (a), (g) 0_1^+, (b), (h) 2_1^+, (c), (i) 0_2^+, (d), (j) 2_2^+, (e), (k) 1_1^-, and (f), (l) 3_1^- states for the considered Se, Kr, Sr, Zr, and Mo nuclei.
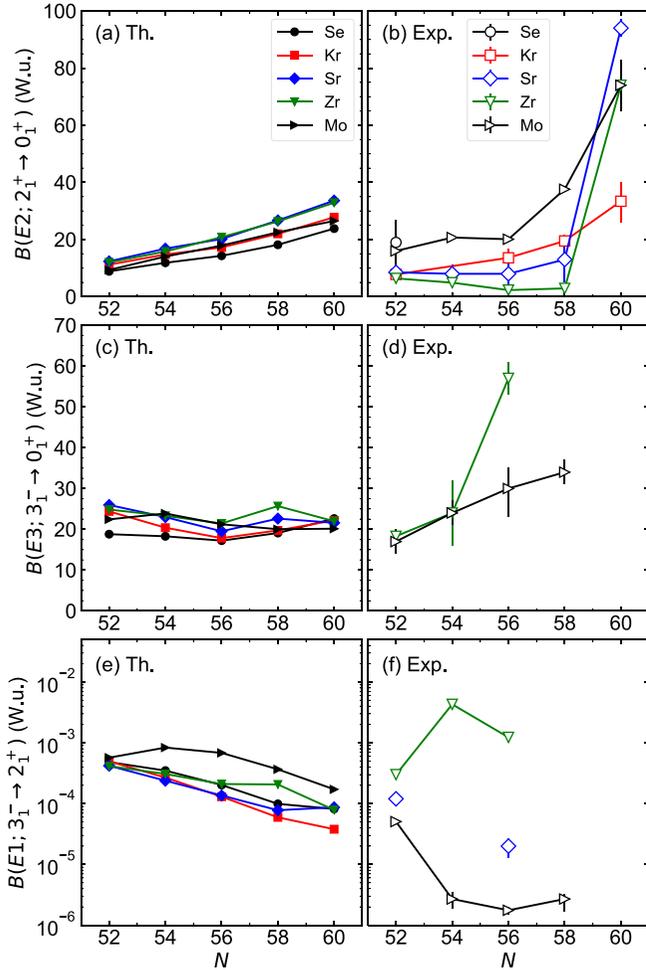
FIG. 9. Evolution of calculated and experimental (a), (b) $B(E2; 2_1^+ \rightarrow 0_1^+)$, (c), (d) $B(E3; 3_1^- \rightarrow 0_1^+)$, and (e), (f) $B(E1; 3_1^- \rightarrow 2_1^+)$ transition strengths in Weisskopf units (W.u.) for the Se, Kr, Sr, Zr, and Mo isotopes with $52 \leqslant N \leqslant 60$. The experimental data are adopted from Refs. [13,15,83,90–93]. Note that a lower limit is shown for the experimental $B(E1)$ value for ^{90}Sr in panel (f).

FIG. 10. Predicted and experimental low-energy positive- and negative-parity spectra for ^{92}Kr. The experimental data are taken from Ref. [12].

the neutron major shell in the Mo isotopes. The $B(E3; 3_1^- \rightarrow 0_1^+)$ rates predicted by the *sdf*-IBM-2 calculation are approximately within the range 20–30 W.u. for all the studied isotopic chains. Note, however, that the calculated values for the Zr and Mo chains are virtually constant against N, being at variance with the observed systematic.

The $B(E1; 3_1^- \rightarrow 2_1^+)$ transition rate is also a relevant quantity to the octupole deformation. There are some data available. Especially, recent measurements for ^{94}Kr and ^{96}Kr suggested the 1350 and 1390 keV decays, respectively, of the 3^- to 2_1^+ states [16]. The calculated $B(E1; 3_1^- \rightarrow 2_1^+)$ values shown in Fig. 9(e) are large near the neutron $N = 50$ major shell gap, and decrease rather rapidly with N toward $N = 60$. The measured $B(E1; 3_1^- \rightarrow 2_1^+)$ values seem to be quite different from one isotopic chain to another, whereas the present calculation gives rather similar values and systematic behaviors among the five isotopic chains. One should also note that, since the $E1$ mode is more of single-particle nature

than the $E2$ and $E3$ ones, the *sdf*-IBM descriptions in general, which consist only of collective degrees of freedom, may not give meaningful predictions for the $E1$ transition properties. For a more reliable IBM description of the $E1$ transition properties, the dipole p bosons with spin and parity $J = 1^-$ could be introduced as additional degrees of freedom to the boson model space [40–42]. This extension, however, lies beyond the scope of the present theoretical analysis.

F. Low-energy spectra for Kr nuclei

Figures 10–12 show detailed low-energy spectra for the neutron-rich isotopes ^{92}Kr, ^{94}Kr, and ^{96}Kr, respectively. The positive-parity part of the level scheme consist of the states in the $K = 0_1^+$ ground-state band and states not classified into bands. For the negative-parity part only the spectra for the odd-spin states are shown.

The ^{92}Kr nucleus corresponds to the octupole neutron magic number $N = 56$, and the corresponding β_2-β_3 potential-energy surface is soft in β_3 deformation (cf. Figs. 1 and 3). As one sees in Fig. 10, the calculation reproduces well the observed $K = 0_1^+$ band and predicts the 2_2^+ states near the 4_1^+ state, which is considered as the bandhead of the quasi-γ or $K = 2_2^+$ band that comprises the 4_2^+, 3_1^+, and 5_1^+ states. The near degeneracy of the members of the quasi-γ band, i.e., 3_1^+ and 4_2^+, indicates the O(6)-like level structure [94]. The 0_2^+ and 2_3^+ states predicted by the calculation are part of the $K = 0_2^+$ band. The mapped *sdf*-IBM-2 gives the low-lying 3_1^- state at around the excitation energy $E_x = 1.5$ MeV, below the 4_1^+ state. Remember that, among the considered Kr isotopes, the lowest 3_1^- level is obtained for ^{92}Kr in the present calculation [cf. Fig. 7(b)].

Similar results to ^{92}Kr are obtained for the ^{94}Kr (Fig. 11) and ^{96}Kr (Fig. 12). In these two nuclei, the *sdf*-IBM-2 en-
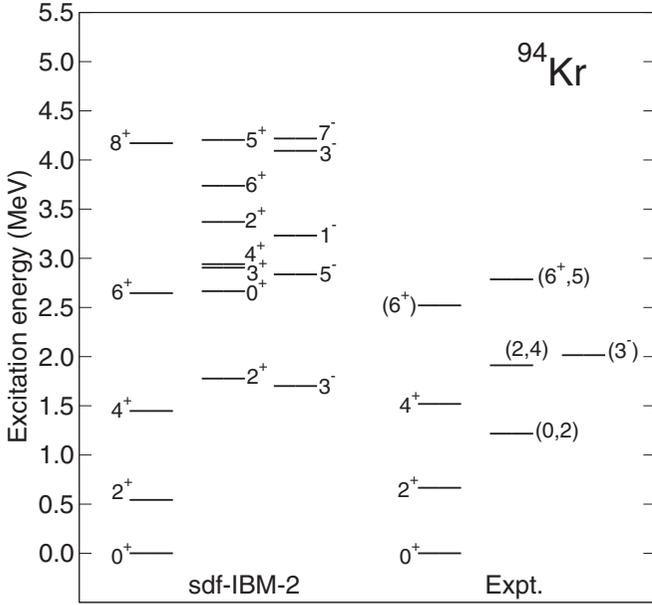
FIG. 11. Same as Fig. 10, but for ^{94}Kr. The experimental data are taken from Ref. [16].

ergy spectra for the $K = 0_1^+$ band looks rather rotational as compared with the experimental counterparts, in such a way that the calculated 2_1^+ energy level is more compressed. The calculated spectra for the positive-parity nonyrast bands in ^{94,96}Kr are also rather high with respect to the $K = 0_1^+$ band, and especially for ^{96}Kr, overestimate the observed nonyrast levels. The calculated 3_1^- excitation energies for both ^{94}Kr and ^{96}Kr are, however, in a good agreement with the experimental values [16], 2015 and 1944 keV, respectively.

Table I lists the predicted $B(E2)$, $B(M1)$, $B(E1)$, and $B(E3)$ transition strengths, and electric-quadrupole $Q(I)$ and
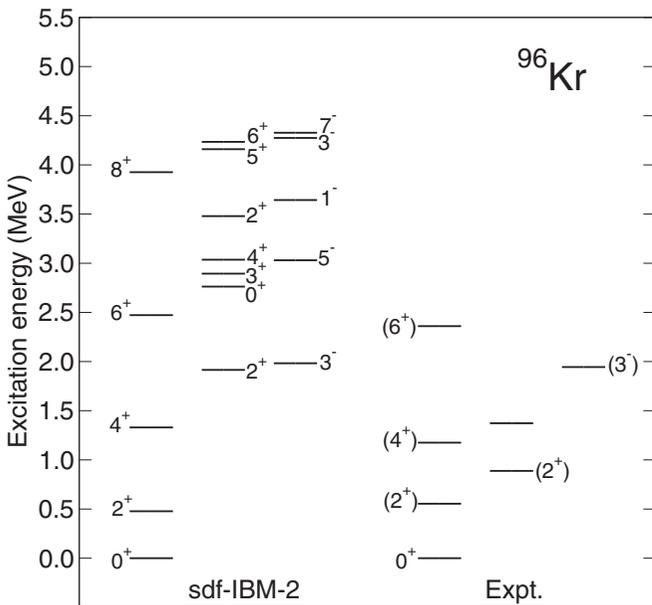
FIG. 12. Same as Fig. 10, but for ^{96}Kr. The experimental data are taken from Ref. [16].

TABLE I. Calculated $B(E2)$, $B(M1)$, $B(E1)$, and $B(E3)$ values (in W.u.), and electric quadrupole $Q(I)$ (in eb) and magnetic dipole $\mu(I)$ (in μ_N) moments for ^{92,94,96}Kr.

	^{92}Kr	^{94}Kr	^{96}Kr
$B(E2; 2_1^+ \rightarrow 0_1^+)$	17	22	28
$B(E2; 4_1^+ \rightarrow 2_1^+)$	24	31	40
$B(E2; 6_1^+ \rightarrow 4_1^+)$	25	34	43
$B(E2; 0_2^+ \rightarrow 2_1^+)$	0.021	0.46	2
$B(E2; 0_2^+ \rightarrow 2_2^+)$	19	29	32
$B(E2; 2_2^+ \rightarrow 2_1^+)$	19	16	14
$B(E2; 3_1^+ \rightarrow 2_2^+)$	18	23	30
$B(E2; 4_2^+ \rightarrow 2_1^+)$	0.11	0.08	0.084
$B(E2; 4_2^+ \rightarrow 2_2^+)$	14	18	22
$B(E2; 4_2^+ \rightarrow 3_1^+)$	1.5	4.6	10
$B(E2; 4_2^+ \rightarrow 4_1^+)$	10	10	9.9
$B(E2; 3_2^- \rightarrow 3_1^-)$	0.16	0.036	0.011
$B(E2; 5_1^- \rightarrow 3_1^-)$	7.2	8.5	11
$B(E2; 7_1^- \rightarrow 5_1^-)$	12	15	21
$B(E2; 9_1^- \rightarrow 7_1^-)$	0.031	18	25
$B(M1; 2_2^+ \rightarrow 2_1^+)$	0.00046	0.00028	0.00015
$B(M1; 3_1^+ \rightarrow 2_2^+)$	0.00086	0.0004	0.00032
$B(M1; 4_2^+ \rightarrow 4_1^+)$	0.0018	0.0011	0.0006
$B(M1; 4_2^+ \rightarrow 3_1^+)$	1.8×10^{-5}	9.7×10^{-6}	6.0×10^{-5}
$B(M1; 3_2^- \rightarrow 3_1^-)$	0.015	0.011	0.011
$B(E1; 1_1^- \rightarrow 0_1^+)$	7.8×10^{-5}	7.6×10^{-5}	9.9×10^{-5}
$B(E1; 1_1^- \rightarrow 2_1^+)$	1.0×10^{-5}	6.9×10^{-6}	3.4×10^{-6}
$B(E1; 3_1^- \rightarrow 2_1^+)$	1.3×10^{-4}	5.9×10^{-5}	3.8×10^{-5}
$B(E1; 3_1^- \rightarrow 4_1^+)$	1.2×10^{-7}	5.1×10^{-7}	1.0×10^{-6}
$B(E1; 5_1^- \rightarrow 4_1^+)$	3.7×10^{-4}	2.1×10^{-4}	1.6×10^{-4}
$B(E1; 5_1^- \rightarrow 6_1^+)$	1.0×10^{-6}	1.3×10^{-6}	4.3×10^{-6}
$B(E1; 7_1^- \rightarrow 6_1^+)$	7.9×10^{-4}	5.3×10^{-4}	4.5×10^{-4}
$B(E3; 3_1^- \rightarrow 0_1^+)$	18	20	22
$B(E3; 3_1^- \rightarrow 2_1^+)$	41	43	44
$B(E3; 5_1^- \rightarrow 2_1^+)$	11	10	11
$B(E3; 5_1^- \rightarrow 4_1^+)$	34	39	42
$B(E3; 7_1^- \rightarrow 4_1^+)$	9.8	8.6	9.9
$B(E3; 7_1^- \rightarrow 6_1^+)$	29	34	37
$Q(2_1^+)$	0.19	0.34	0.45
$\mu(2_1^+)$	0.37	0.32	0.32

magnetic-dipole $\mu(I)$ moments for the ^{92,94,96}Kr isotopes. One can see from the table that the calculated values for these electromagnetic properties are basically similar among the three Kr nuclei. The in-band $\Delta I = 2E2$ transitions, i.e., $2_1^+ \rightarrow 0_1^+$, $4_1^+ \rightarrow 2_1^+$, $6_1^+ \rightarrow 4_1^+$, $5_1^- \rightarrow 3_1^-$, and $7_1^- \rightarrow 5_1^-$, as well as the $Q(2_1^+)$ values, gradually increase from ^{92}Kr to ^{96}Kr. These systematics illustrate gradual evolution of quadrupole collectivity. The available experimental data [92], $B(E2; 2_1^+ \rightarrow 0_1^+) = 13.6_{-3.3}^{+2.8}$, $19.5_{-2.1}^{+2.2}$, and $33.4_{-6.7}^{+7.4}$ W.u. for ^{92}Kr, ^{94}Kr, and ^{96}Kr, respectively, are reasonably reproduced by the present sdf-IBM-2 calculation. The data are also available from Ref. [92] for the $Q(2_1^+)$ values, $-0.61_{-0.45}^{+0.53}$ e b and $-0.26_{-0.16}^{+0.19}$ e b, for ^{92}Kr and ^{94}Kr, respectively, are rather at variance with the present theoretical values both in sign and magnitude. The calculated $Q(2_1^+)$ value for ^{96}Kr is, however, within error bar of the experimental one [92], 0.15 ± 0.53 e b. The considered $B(E3)$ values also become gradually larger for
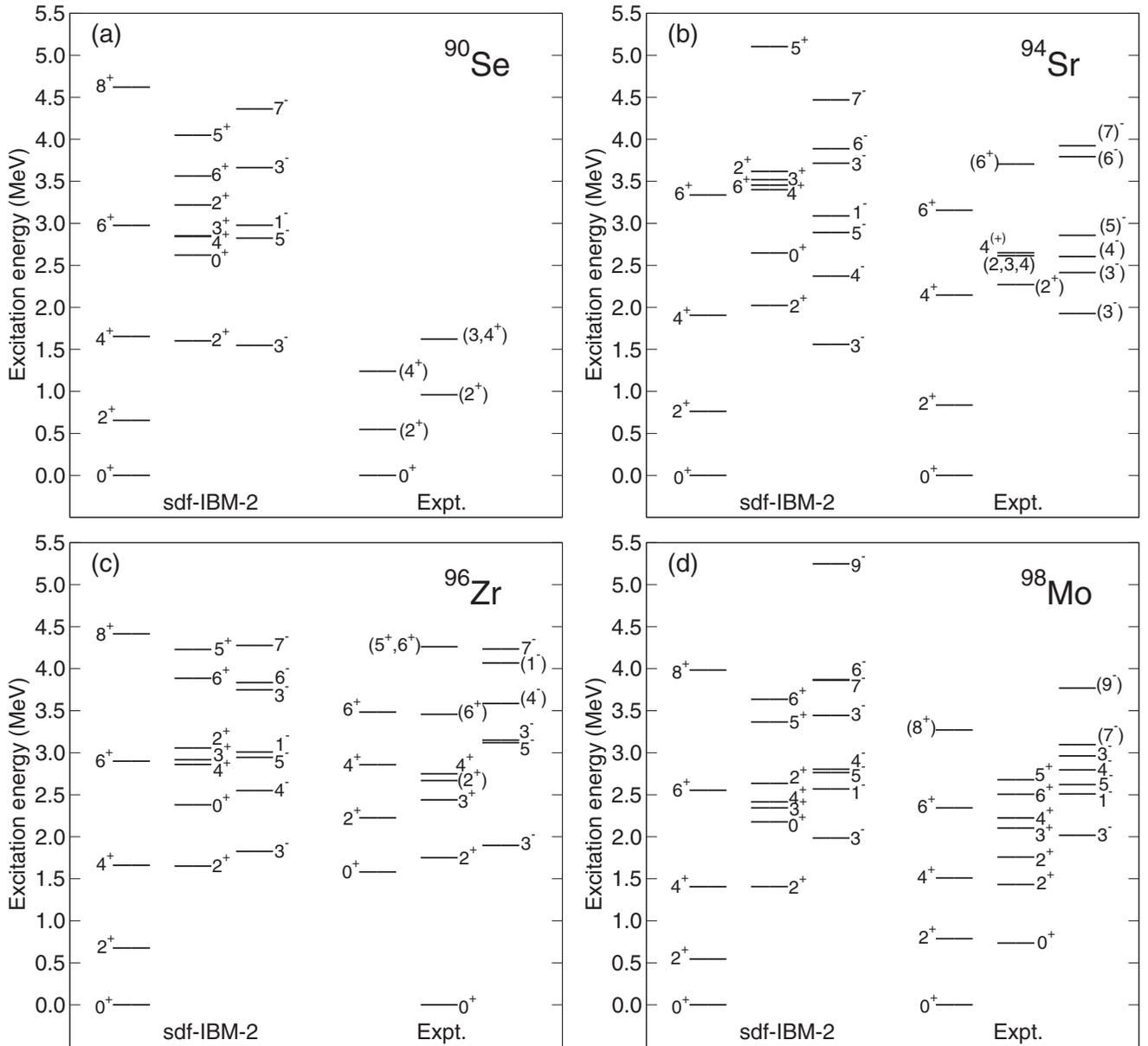
FIG. 13. Same as Fig. 10, but for the $N = 56$ isotones (a) ^{90}Se, (b) ^{94}Sr, (c) ^{96}Zr, and (d) ^{98}Mo. The experimental data are taken from Refs. [85] (^{90}Se), [84] (^{94}Sr), [83] (^{96}Zr), and [10,95] (^{98}Mo).

heavier Kr as the neutron number increases. This is a consequence of the fact that almost constant strength parameters are used for the Kr isotopes (cf. Fig. 5), and thus these transition rates increase only monotonically with the boson number.

For completeness, Table I shows some calculated $B(M1)$ and $B(E1)$ dipole transitions. An interesting feature is that the calculated $B(M1; 3_2^- \rightarrow 3_1^-)$ transition rate is large $\gtrsim 0.01$ W.u., while the corresponding $B(E2)$ value $B(E2; 3_2^- \rightarrow 3_1^-) < 1$ W.u. is small. Experimentally, strong $M1$ transitions from the 3_i^- ($i = 1$ or 2) excited state at $E_x \approx 3.1$ MeV to the 3_1^- state have been suggested in some of the nearly spherical $N = 52$ isotones, ^{92}Zr and ^{94,96}Mo [11], and have been identified as the isovector octupole excitation modes. As for the $B(E1)$ rates, the transitions from the higher-spin negative-parity to lower-spin positive-parity

states are systematically larger than those in the opposite direction, i.e., from the lower-spin negative-parity to higher-spin positive-parity states. Similar tendency has been obtained in the previous sdf-IBM calculations in other mass regions [45,49], and this staggering pattern in the $B(E1)$ rates can be partly attributed to the fact that the model space and the $E1$ transition operator do not include the effect of p-boson degree of freedom. At any rate, experimental data on the transition properties is so scarce for the neutron-rich Kr isotopes that an extensive assessments of the model description and of the quality of the sdf-IBM-2 wave functions remain to be done.

G. Low-energy spectra for $N = 56$ isotones

Figure 13 shows the low-energy-level schemes for the $N = 56$ isotones other than ^{92}Kr, that is, ^{90}Se, ^{94}Sr, ^{96}Zr, and ^{98}Mo.

TABLE II. Same as Table I, but for ^{90}Se and ^{94}Sr.

	^{90}Se	^{94}Sr
$B(E2; 2_1^+ \to 0_1^+)$	14	20
$B(E2; 2_2^+ \to 0_1^+)$	0.29	0.68
$B(E2; 2_2^+ \to 2_1^+)$	18	21
$B(E2; 4_1^+ \to 2_1^+)$	19	29
$B(E2; 4_2^+ \to 2_1^+)$	0.047	0.14
$B(E2; 4_2^+ \to 2_2^+)$	11	17
$B(E2; 4_2^+ \to 4_1^+)$	9.3	12
$B(E2; 3_1^+ \to 2_1^+)$	0.24	0.86
$B(E2; 3_1^+ \to 2_2^+)$	14	21
$B(E2; 3_2^- \to 3_1^-)$	0.015	0.54
$B(M1; 2_2^+ \to 2_1^+)$	0.001	0.00039
$B(M1; 3_1^+ \to 2_1^+)$	0.00015	0.00012
$B(M1; 3_1^+ \to 2_2^+)$	0.0032	0.00037
$B(M1; 4_2^+ \to 4_1^+)$	0.0025	0.0017
$B(M1; 3_2^- \to 3_1^-)$	0.014	0.017
$B(E1; 1_1^- \to 0_1^+)$	1.0×10^{-4}	7.6×10^{-5}
$B(E1; 3_2^- \to 2_1^+)$	1.7×10^{-5}	8.8×10^{-5}
$B(E1; 3_1^- \to 2_1^+)$	2.0×10^{-4}	1.4×10^{-4}
$B(E1; 3_1^- \to 2_2^+)$	5.6×10^{-4}	5.5×10^{-4}
$B(E1; 3_1^- \to 4_1^+)$	4.5×10^{-7}	2.2×10^{-8}
$B(E1; 5_1^- \to 4_1^+)$	5.3×10^{-4}	3.8×10^{-4}
$B(E1; 7_1^- \to 6_1^+)$	1.1×10^{-3}	6.9×10^{-4}
$B(E3; 3_1^- \to 0_1^+)$	17	20
$B(E3; 3_1^- \to 2_1^+)$	42	36
$B(E3; 3_1^- \to 4_1^+)$	12	6.6
$B(E3; 5_1^- \to 2_1^+)$	12	13
$B(E3; 5_1^- \to 4_1^+)$	33	31
$B(E3; 7_1^- \to 4_1^+)$	11	12
$B(E3; 7_1^- \to 6_1^+)$	30	19
$Q(2_1^+)$	0.087	0.24
$\mu(2_1^+)$	0.31	0.39

The nucleus ^{90}Se corresponds to both the neutron $N = 56$ and proton $Z = 34$ empirical octupole magic numbers. The SCMF result for this nucleus suggests that it is more or less soft in the octupole β_3 deformation (see Fig. 1). The predicted low-energy spectrum in Fig. 13 for ^{90}Se resembles the one for the neighboring isotone ^{92}Kr. For instance, the 4_1^+, 2_2^+, and 3_1^- states are nearly degenerate at $E_x \approx 1.5$ MeV. In addition, the calculation predicts the 3_1^- excitation energy to be $E_x = 1597$ keV, while, experimentally [85], there is a level at $E_x = 1600$ keV with tentatively assigned spin and parity $(3, 4^+)$. As compared with the experimental data [85], the predicted $K = 0_1^+$ band is rather stretched in energy. Some calculated $B(E2)$, $B(M1)$, $B(E1)$, and $B(E3)$ transition rates and the $Q(I)$ and $\mu(I)$ moments are listed in Table II. Note that the experimental data for the electromagnetic transition properties are not available for this nucleus.

For ^{94}Sr, an agreement between the *sdf*-IBM-2 and the experimental [83,84] low-energy spectra is generally satisfactory, particularly for the $K = 0_1^+$ band, the bandhead energy of the quasi-γ band, i.e., 2_2^+, and many of the negative-parity states. Note that the 6_2^+ state is calculated to be particularly low in energy, being close to the 6_1^+

one. The approximate degeneracy arises probably because a large fraction of the f-boson components is admixed into its wave function. The calculation gives the low-lying 3_1^- state below the 4_1^+ state, and also reproduces the even-spin negative-parity states 4^- and 6^-. The predicted 3_2^- energy is, however, much higher than the experimental one. Note that the spin and parity of the 3_1^- and 3_2^- states are not firmly established experimentally. Predicted $B(E2)$, $B(M1)$, $B(E1)$, and $B(E3)$ transition rates and the $Q(I)$ and $\mu(I)$ moments for ^{94}Sr are summarized in Table II. The available experimental data [83] are $B(E2; 2_1^+ \to 0_1^+) = 8 \pm 4$, $B(E1; 3_2^- \to 2_1^+) = (2.0 \pm 0.7) \times 10^{-5}$, and $B(E1; 5_1^- \to 4_1^+) = (1.5 \pm 0.7) \times 10^{-5}$ W.u.

The ^{96}Zr nucleus corresponds to the doubly subshell closure of $N = 56$ and $Z = 40$. As already shown in Fig. 6(d), the *sdf*-IBM-2 only produces a collective band structure for the positive-parity yrast band, whereas, experimentally [93], the first-excited state is the 0_2^+ state at $E_x = 1582$ keV and the high-lying 2_1^+ state is found at 1750 keV. It was shown by the Monte Carlo shell-model calculation [93,96] that this 0_2^+ is likely to arise from the intruder deformed configuration. The 0_2^+ state obtained by the present *sdf*-IBM-2 calculation is quite different in nature, since in the present framework the intruder excitations and the subsequent configuration mixing between the normal and intruder states are not taken into account. However, the mapped *sdf*-IBM-2 calculation generally provides a reasonable description of the observed negative-parity levels.

The electromagnetic transition properties of the low-lying states in ^{96}Zr computed by the mapped *sdf*-IBM-2 Hamiltonian are shown in Table III, together with the experimental data [83,93]. Some disagreements between the calculated and experimental $E2$ transition properties for ^{96}Zr, especially those related to the positive-parity states, are mainly due to the lack of the intruder configuration in the model. The predicted $B(E3)$ values for the transitions from the odd-spin negative-parity states are noticeably large, particularly, for the $\Delta I = 1 E3$ transitions.

The predicted low-energy spectrum for ^{98}Mo, shown in Fig. 13(d), is basically similar to the one for ^{96}Zr. Comparing with the experimental data [10,83,95], the predicted $K = 0_1^+$ band suggests a slightly stronger quadrupole collectivity with the ratio $R_{4/2} = 2.58$. The calculated 0_2^+ excitation energy $E_x(0_2^+) = 2178$ keV is much higher than the experimental counterpart $E_x(0_2^+) = 735$ keV. Experimentally, the 0_2^+ state is also the first excited state of ^{98}Mo. As already remarked, the 0_2^+ level could be lowered by the inclusion of the configuration mixing between the normal and intruder states. A previous mapped IBM-2 configuration-mixing calculation, which is based on a Skyrme-type EDF, showed [95] that the coexistence of a nearly spherical prolate and γ-soft prolate SCMF minima is present in ^{98}Mo and that the 0_2^+ state is characterized by the strong mixing between the nearly spherical normal configuration and the deformed intruder configuration arising from the proton $2p$-$2h$ excitation across the $Z = 40$ subshell closure. On the other hand, the observed negative-parity states up to the 4_1^- state are reasonably reproduced. Some relevant electromagnetic properties for ^{98}Mo resulting from the

TABLE III. $B(E2)$, $B(M1)$, $B(E1)$, and $B(E3)$ transition rates (in W.u.), and the electric quadrupole $Q(I)$ (in e b), and magnetic dipole $\mu(I)$ (in μ_N) moments, predicted by the mapped sdf-IBM-2 for ^{96}Zr in comparison with the available experimental data [83,93].

	sdf-IBM-2	Experiment
$B(E2; 0_3^+ \to 2_2^+)$	11	34 ± 9
$B(E2; 2_1^+ \to 0_1^+)$	21	2.3 ± 0.3
$B(E2; 2_2^+ \to 2_1^+)$	26	>0.16
$B(E2; 2_2^+ \to 0_2^+)$	4.5	36 ± 11
$B(E2; 2_2^+ \to 0_1^+)$	0.31	0.26 ± 0.08
$B(E2; 2_3^+ \to 2_1^+)$	0.079	$(5.0 \pm 0.7)E+1$
$B(E2; 3_1^+ \to 2_1^+)$	0.43	$0.1_{-0.1}^{+0.3}$
$B(E2; 4_1^+ \to 2_1^+)$	0.0016	56_{-44}^{+20}
$B(E2; 4_1^+ \to 2_2^+)$	29	16_{-13}^{+5}
$B(E2; 4_2^+ \to 2_1^+)$	0.068	
$B(E2; 4_2^+ \to 2_2^+)$	17	<1.6
$B(E2; 4_3^+ \to 2_1^+)$	0.00042	$0.4_{-0.4}^{+0.4}$
$B(E2; 3_2^- \to 3_1^-)$	1.7	<4.2
$B(E2; 5_1^- \to 3_1^-)$	10	14_{-14}^{+5}
$B(M1; 2_2^+ \to 2_1^+)$	0.00082	0.14 ± 0.05
$B(M1; 2_3^+ \to 2_1^+)$	0.022	0.04 ± 0.06
$B(M1; 3_1^+ \to 2_1^+)$	9.0×10^{-5}	$0.18_{-0.09}^{+0.05}$
$B(M1; 3_2^- \to 3_1^-)$	0.011	<0.0027
$B(E1; 1_1^- \to 0_1^+)$	1.1×10^{-4}	
$B(E1; 2_2^- \to 3_1^-)$	7.1×10^{-4}	$(2.8 \pm 0.9) \times 10^{-3}$
$B(E1; 2_3^+ \to 3_1^-)$	1.4×10^{-5}	$(0.0007_{-0.0007}^{+0.0004})$
$B(E1; 4_1^+ \to 3_1^-)$	5.1×10^{-7}	$(7.0_{-0.6}^{+0.3})E-5$
$B(E1; 4_3^+ \to 3_1^-)$	8.3×10^{-7}	<0.00010
$B(E1; 3_1^- \to 2_1^+)$	2.1×10^{-4}	0.00123 ± 0.00010
$B(E1; 3_2^- \to 3_1^+)$	1.8×10^{-4}	<0.00100
$B(E1; 5_1^- \to 4_1^+)$	5.3×10^{-4}	
$B(E1; 7_1^- \to 6_1^+)$	1.0×10^{-3}	
$B(E3; 3_1^- \to 0_1^+)$	21	57 ± 4
$B(E3; 3_1^- \to 0_2^+)$	0.069	
$B(E3; 3_1^- \to 2_1^+)$	38	
$B(E3; 5_1^- \to 2_1^+)$	17	
$B(E3; 5_1^- \to 4_1^+)$	32	
$B(E3; 7_1^- \to 4_1^+)$	15	
$B(E3; 7_1^- \to 6_1^+)$	28	
$Q(2_1^+)$	0.17	
$Q(3_1^-)$	-0.42	$+2.9 \pm 0.5$
$\mu(2_1^+)$	0.4	$+0.06 \pm 0.14$

TABLE IV. Same as Table III, but for ^{98}Mo. The experimental data are taken from Refs. [10,83,95].

	sdf-IBM-2	Experiment
$B(E2; 2_1^+ \to 0_1^+)$	18	20.1 ± 0.4
$B(E2; 2_1^+ \to 0_2^+)$	0.35	$9.7_{-2.5}^{+1.0}$
$B(E2; 2_2^+ \to 0_1^+)$	0.36	$1.02_{-0.12}^{+0.15}$
$B(E2; 2_2^+ \to 0_2^+)$	4.3	$2.3_{-0.4}^{+0.5}$
$B(E2; 2_2^+ \to 2_1^+)$	17	48_{-8}^{+9}
$B(E2; 2_3^+ \to 4_1^+)$	0.037	14 ± 4
$B(E2; 2_3^+ \to 2_2^+)$	0.11	<22
$B(E2; 2_3^+ \to 2_1^+)$	0.19	3.0 ± 0.7
$B(E2; 2_3^+ \to 0_2^+)$	0.36	$7.5_{-0.5}^{+0.6}$
$B(E2; 2_3^+ \to 0_1^+)$	0.0033	$0.032_{-0.006}^{+0.007}$
$B(E2; 2_4^+ \to 2_1^+)$	0.00031	>0.49
$B(E2; 4_1^+ \to 2_1^+)$	25	$42.3_{-0.8}^{+0.9}$
$B(E2; 4_1^+ \to 2_2^+)$	0.023	$15.2_{-3.0}^{+3.3}$
$B(E2; 6_1^+ \to 4_1^+)$	26	10.1 ± 0.4
$B(E2; 3_2^- \to 3_1^-)$	0.5	
$B(M1; 2_2^+ \to 2_1^+)$	0.0021	$0.0073_{-0.0017}^{+0.0023}$
$B(M1; 2_3^+ \to 2_2^+)$	0.00013	$0.0157_{-0.0034}^{+0.0027}$
$B(M1; 2_3^+ \to 2_1^+)$	0.023	$0.0032_{-0.0007}^{+0.0008}$
$B(M1; 2_4^+ \to 2_1^+)$	0.0016	>0.019
$B(M1; 2_5^+ \to 2_2^+)$	0.0019	>0.054
$B(M1; 3_2^- \to 3_1^-)$	0.013	
$B(E1; 1_1^- \to 0_1^+)$	2.5×10^{-4}	
$B(E1; 3_1^- \to 2_3^+)$	1.9×10^{-5}	$(4.9_{-0.7}^{+0.9}) \times 10^{-5}$
$B(E1; 3_1^- \to 4_1^+)$	4.0×10^{-6}	$(1.02_{-0.24}^{+0.31}) \times 10^{-6}$
$B(E1; 3_1^- \to 2_2^+)$	1.8×10^{-4}	$<5.7 \times 10^{-8}$
$B(E1; 3_1^- \to 2_1^+)$	6.8×10^{-4}	$(1.76_{-0.22}^{+0.28}) \times 10^{-6}$
$B(E1; 3_2^- \to 2_1^+)$	3.8×10^{-5}	
$B(E1; 3_2^- \to 2_2^+)$	1.5×10^{-4}	
$B(E1; 5_1^- \to 4_1^+)$	1.3×10^{-3}	
$B(E1; 7_1^- \to 6_1^+)$	1.9×10^{-3}	
$B(E3; 3_1^- \to 0_2^+)$	0.038	<58
$B(E3; 3_1^- \to 0_1^+)$	21	30_{-5}^{+7}
$B(E3; 3_1^- \to 2_1^+)$	25	
$B(E3; 3_1^- \to 2_2^+)$	5.2	
$B(E3; 3_2^- \to 2_1^+)$	0.17	
$B(E3; 3_2^- \to 2_2^+)$	1.8	
$B(E3; 5_1^- \to 2_1^+)$	26	
$B(E3; 5_1^- \to 4_1^+)$	19	
$B(E3; 7_1^- \to 4_1^+)$	25	
$B(E3; 7_1^- \to 6_1^+)$	18	
$Q(2_1^+)$	-0.25	-0.26 ± 0.09
$\mu(2_1^+)$	0.31	$+0.97 \pm 0.06$

mapped sdf-IBM-2 calculation are shown in Table IV in comparison to the available data [83,95]. The agreement with the experimental data is fair. The calculation suggests strong $\Delta I = 3 E3$ transitions of the odd-spin negative-parity to the even-spin positive-parity yrast states.

IV. CONCLUDING REMARKS

Octupole correlations and the related spectroscopic properties of the neutron-rich $A \approx 100$ nuclei near the empirical octupole magic numbers $Z = 34$ and $N = 56$ have been investigated based on the nuclear density-functional theory and the mapped sdf-IBM-2 framework. The axially symmetric quadrupole and octupole constrained SCMF calculations us-

ing the relativistic DD-PC1 EDF and the separable pairing force of finite range have been carried out to provide the potential-energy surfaces for the considered even-even nuclei $^{86-94}$Se, $^{88-96}$Kr, $^{90-98}$Sr, $^{92-100}$Zr, and $^{94-102}$Mo as functions of the β_2 and β_3 deformations. At the SCMF level, no nonzero β_3 minimum was obtained on the β_2-β_3 energy surfaces, whereas the potential becomes soft in the β_3 deformation around the neutron number $N = 56$ for each of the considered isotopic chains. The excitation spectra for the low-lying states with both parities and the electromagnetic transition rates have been computed by the diagonalization of the sdf-IBM-2

Hamiltonian with the strength parameters determined by mapping the SCMF energy surface onto the expectation value of the Hamiltonian in the boson condensate state.

Evolution of the predicted positive-parity yrast spectra has indicated a smooth onset of quadrupole collectivity in the Se, Kr, and Mo isotopes, and an abrupt nuclear structural change at $N \approx 60$ in the Sr and Zr chains, as empirically suggested. The present theoretical analysis put much emphasis on the description of the negative-parity states. The predicted negative-parity odd-spin states show a parabolic dependence on N centered around $N = 56$ at which the corresponding β_2-β_3 energy surface becomes softest along the β_3 direction. The lowest negative-parity state 3_1^- has been predicted to be typically at the excitation energy $E_x \approx 1.5$–2.5 MeV, in a reasonable agreement with experiment. The detailed comparisons have been made between the calculated and experimental low-lying energy levels and transition properties for the $N = 56$ isotones and some of the neutron-rich Kr nuclei that are of interest for recent measurements. The present calculation has produced finite $E3$ transitions from the odd-spin negative-parity states to the ground-state band. These findings indicate the relevance of the octupole degrees of freedom in the description of the low-energy negative-parity states in the neutron-rich nuclei near the octupole magic numbers $N = 56$ and $Z = 34$ within the framework of the sdf-IBM-2.

For a more complete description of the low-energy states with both parities and their spectroscopy in this mass region, some extensions of the model will be required. In particular, the sdf-IBM-2 Hamiltonian has been here determined by the constrained SCMF calculations based only on the axially symmetric shape degrees of freedom. On the other hand, the studied neutron-rich nuclei should have a more complex low-lying structure characterized, e.g., by the nonaxial deformation and shape coexistence. Indeed, it has been revealed that the mapped sdf-IBM-2 employed in this paper is not able to describe the low-lying 0_2^+ state and the band built on it for the $N > 56$ nuclei. The model would need to be extended in such a way that it simultaneously handles the octupole boson degrees of freedom, the triaxial deformation, and the intruder states and configuration mixing. Work along this direction is in progress and will be reported elsewhere.

[1] K. Heyde and J. L. Wood, Rev. Mod. Phys. **83**, 1467 (2011).

[2] P. Cejnar, J. Jolie, and R. F. Casten, Rev. Mod. Phys. **82**, 2155 (2010).

[3] P. A. Butler and W. Nazarewicz, Rev. Mod. Phys. **68**, 349 (1996).

[4] P. A. Butler, J. Phys. G **43**, 073002 (2016).

[5] L. P. Gaffney, P. A. Butler, M. Scheck, A. B. Hayes, F. Wenander, M. Albers, B. Bastin, C. Bauer, A. Blazhev, S. Bönig, N. Bree, J. Cederkäll, T. Chupp, D. Cline, T. E. Cocolios, T. Davinson, H. D. Witte, J. Diriken, T. Grahn, A. Herzan *et al.*, Nature (London) **497**, 199 (2013).

[6] M. M. R. Chishti, D. O'Donnell, G. Battaglia, M. Bowry, D. A. Jaroszynski, B. S. N. Singh, M. Scheck, P. Spagnoletti, and J. F. Smith, Nat. Phys. **16**, 853 (2020).

[7] B. Bucher, S. Zhu, C. Y. Wu, R. V. F. Janssens, D. Cline, A. B. Hayes, M. Albers, A. D. Ayangeakaa, P. A. Butler, C. M. Campbell, M. P. Carpenter, C. J. Chiara, J. A. Clark, H. L. Crawford, M. Cromaz, H. M. David, C. Dickerson, E. T. Gregor, J. Harker, C. R. Hoffman *et al.*, Phys. Rev. Lett. **116**, 112503 (2016).

[8] B. Bucher, S. Zhu, C. Y. Wu, R. V. F. Janssens, R. N. Bernard, L. M. Robledo, T. R. Rodríguez, D. Cline, A. B. Hayes, A. D. Ayangeakaa, M. Q. Buckner, C. M. Campbell, M. P. Carpenter, J. A. Clark, H. L. Crawford, H. M. David, C. Dickerson, J. Harker, C. R. Hoffman, B. P. Kay *et al.*, Phys. Rev. Lett. **118**, 152504 (2017).

[9] T. Rzaca-Urban, W. Urban, A. Kaczor, J. L. Durell, M. J. Leddy, M. A. Jones, W. R. Phillips, A. G. Smith, B. J. Varley, I. Ahmad, L. R. Morss, M. Bentaleb, E. Lubkiewicz, and N. Schulz, Eur. Phys. J. A **9**, 165 (2000).

[10] S. Lalkovski, S. Ilieva, A. Minkova, N. Minkov, T. Kutsarova, A. Lopez-Martens, A. Korichi, H. Hübel, A. Görgen, A. Jansen, G. Schönwasser, B. Herskind, M. Bergström, and Z. Podolyák, Phys. Rev. C **75**, 014314 (2007).

[11] M. Scheck, P. A. Butler, C. Fransen, V. Werner, and S. W. Yates, Phys. Rev. C **81**, 064305 (2010).

[12] K. Li, J. H. Hamilton, A. V. Ramayya, S. H. Liu, X. Q. Zhang, N. T. Brewer, J. K. Hwang, C. Goodin, S. J. Zhu, Y. X. Luo, J. O. Rasmussen, I. Y. Lee, S. C. Wu, R. Donangelo, A. V. Daniel, G. M. Ter-Akopian, Y. T. Oganessian, A. Unzhakova, J. D. Cole, W. C. Ma *et al.*, Int. J. Mod. Phys. E **20**, 1825 (2011).

[13] E. T. Gregor, M. Scheck, R. Chapman, L. P. Gaffney, J. Keatings, K. R. Mashtakov, D. O'Donnell, J. F. Smith, P. Spagnoletti, M. Thürauf, V. Werner, and C. Wiseman, Eur. Phys. J. A **53**, 50 (2017).

[14] J. Dudouet, A. Lemasson, G. Duchêne, M. Rejmund, E. Clément, C. Michelagnoli, F. Didierjean, A. Korichi, G. Maquart, O. Stezowski, C. Lizarazo, R. M. Pérez-Vidal, C. Andreoiu, G. de Angelis, A. Astier, C. Delafosse, I. Deloncle, Z. Dombradi, G. de France, A. Gadea *et al.*, Phys. Rev. Lett. **118**, 162501 (2017).

[15] E. T. Gregor, N. N. Arsenyev, M. Scheck, T. M. Shneidman, M. Thürauf, C. Bernards, A. Blanc, R. Chapman, F. Drouet, A. A. Dzhioev, G. de France, M. Jentschel, J. Jolie, J. M. Keatings, T. Kröll, U. Köster, R. Leguillon, K. R. Mashtakov, P. Mutti, D. O'Donnell *et al.*, J. Phys. G **46**, 075101 (2019).

[16] R.-B. Gerst, A. Blazhev, K. Moschner, P. Doornenbal, A. Obertelli, K. Nomura, J.-P. Ebran, S. Hilaire, J. Libert, G. Authelet, H. Baba, D. Calvet, F. Château, S. Chen, A. Corsi, A. Delbart, J.-M. Gheller, A. Giganon, A. Gillibert, V. Lapoux *et al.*, Phys. Rev. C **105**, 024302 (2022).

[17] W. Nazarewicz, P. Olanders, I. Ragnarsson, J. Dudek, G. A. Leander, P. Möller, and E. Ruchowsa, Nucl. Phys. A **429**, 269 (1984).

[18] G. Leander, W. Nazarewicz, P. Olanders, I. Ragnarsson, and J. Dudek, Phys. Lett. B **152**, 284 (1985).

[19] P. Möller, R. Bengtsson, B. Carlsson, P. Olivius, T. Ichikawa, H. Sagawa, and A. Iwamoto, At. Data Nucl. Data Tables **94**, 758 (2008).

[20] P. Bonche, P.-H. Heenen, H. Flocard, and D. Vautherin, Phys. Lett. B **175**, 387 (1986).

[21] P.-H. Heenen, J. Skalski, P. Bonche, and H. Flocard, Phys. Rev. C **50**, 802 (1994).

[22] L. Robledo, J. Egido, J. Berger, and M. Girod, Phys. Lett. B **187**, 223 (1987).

[23] J. Egido and L. Robledo, Nucl. Phys. A **545**, 589 (1992).

[24] L. M. Robledo, M. Baldo, P. Schuck, and X. Viñas, Phys. Rev. C **81**, 034315 (2010).

[25] L. M. Robledo and G. F. Bertsch, Phys. Rev. C **84**, 054302 (2011).

[26] Z. P. Li, B. Y. Song, J. M. Yao, D. Vretenar, and J. Meng, Phys. Lett. B **726**, 866 (2013).

[27] L. M. Robledo and P. A. Butler, Phys. Rev. C **88**, 051302(R) (2013).

[28] J. M. Yao, E. F. Zhou, and Z. P. Li, Phys. Rev. C **92**, 041304(R) (2015).

[29] R. N. Bernard, L. M. Robledo, and T. R. Rodríguez, Phys. Rev. C **93**, 061302(R) (2016).

[30] S. Y. Xia, H. Tao, Y. Lu, Z. P. Li, T. Nikšić, and D. Vretenar, Phys. Rev. C **96**, 054303 (2017).

[31] S. E. Agbemava and A. V. Afanasjev, Phys. Rev. C **96**, 024301 (2017).

[32] S. Ebata and T. Nakatsukasa, Phys. Scr. **92**, 064005 (2017).

[33] P. Marević, J.-P. Ebran, E. Khan, T. Nikšić, and D. Vretenar, Phys. Rev. C **97**, 024334 (2018).

[34] L. M. Robledo, T. R. Rodríguez, and R. R. Rodríguez-Guzmán, J. Phys. G **46**, 013001 (2019).

[35] Y. Cao, S. E. Agbemava, A. V. Afanasjev, W. Nazarewicz, and E. Olsen, Phys. Rev. C **102**, 024311 (2020).

[36] R. Rodríguez-Guzmán, Y. M. Humadi, and L. M. Robledo, J. Phys. G **48**, 015103 (2021).

[37] K. Nomura, L. Lotina, T. Nikšić, and D. Vretenar, Phys. Rev. C **103**, 054301 (2021).

[38] J. Engel and F. Iachello, Phys. Rev. Lett. **54**, 1126 (1985).

[39] J. Engel and F. Iachello, Nucl. Phys. A **472**, 61 (1987).

[40] T. Otsuka, Phys. Lett. B **182**, 256 (1986).

[41] T. Otsuka and M. Sugita, Phys. Lett. B **209**, 140 (1988).

[42] M. Sugita, T. Otsuka, and P. von Brentano, Phys. Lett. B **389**, 642 (1996).

[43] D. Kusnezov and F. Iachello, Phys. Lett. B **209**, 420 (1988).

[44] Y. Naotaka, T. Mizusaki, and T. Otsuka, Nucl. Phys. A **559**, 193 (1993).

[45] N. V. Zamfir and D. Kusnezov, Phys. Rev. C **63**, 054306 (2001).

[46] N. A. Smirnova, N. Pietralla, T. Mizusaki, and P. Van Isacker, Nucl. Phys. A **678**, 235 (2000).

[47] N. Pietralla, C. Fransen, A. Gade, N. A. Smirnova, P. von Brentano, V. Werner, and S. W. Yates, Phys. Rev. C **68**, 031305(R) (2003).

[48] K. Nomura, D. Vretenar, and B.-N. Lu, Phys. Rev. C **88**, 021303(R) (2013).

[49] K. Nomura, D. Vretenar, T. Nikšić, and B.-N. Lu, Phys. Rev. C **89**, 024312 (2014).

[50] K. Nomura, R. Rodríguez-Guzmán, and L. M. Robledo, Phys. Rev. C **92**, 014312 (2015).

[51] K. Nomura, R. Rodríguez-Guzmán, Y. M. Humadi, L. M. Robledo, and J. E. García-Ramos, Phys. Rev. C **102**, 064326 (2020).

[52] K. Nomura, R. Rodríguez-Guzmán, L. Robledo, and J. García-Ramos, Phys. Rev. C **103**, 044311 (2021).

[53] K. Nomura, R. Rodríguez-Guzmán, L. M. Robledo, J. E. García-Ramos, and N. C. Hernández, Phys. Rev. C **104**, 044324 (2021).

[54] K. Nomura, R. Rodríguez-Guzmán, and L. M. Robledo, Phys. Rev. C **104**, 054320 (2021).

[55] A. Hennig, M. Spieker, V. Werner, T. Ahn, V. Anagnostatou, N. Cooper, V. Derya, M. Elvers, J. Endres, P. Goddard, A. Heinz, R. O. Hughes, G. Ilie, M. N. Mineva, P. Petkov, S. G. Pickstone, N. Pietralla, D. Radeck, T. J. Ross, D. Savran *et al.*, Phys. Rev. C **90**, 051302(R) (2014).

[56] O. Vallejos and J. Barea, Phys. Rev. C **104**, 014308 (2021).

[57] D. Bonatsos, I. Lenis, N. Minkov, D. Petrellis, and P. Yotov, Phys. Rev. C **71**, 064309 (2005).

[58] D. Lenis and D. Bonatsos, Phys. Lett. B **633**, 474 (2006).

[59] P. G. Bizzeti and A. M. Bizzeti-Sona, Phys. Rev. C **88**, 011305(R) (2013).

[60] D. Bonatsos, A. Martinou, N. Minkov, S. Karampagia, and D. Petrellis, Phys. Rev. C **91**, 054315 (2015).

[61] T. M. Shneidman, G. G. Adamian, N. V. Antonenko, R. V. Jolos, and W. Scheid, Phys. Lett. B **526**, 322 (2002).

[62] T. M. Shneidman, G. G. Adamian, N. V. Antonenko, R. V. Jolos, and W. Scheid, Phys. Rev. C **67**, 014313 (2003).

[63] R. V. Jolos, P. von Brentano, and J. Jolie, Phys. Rev. C **86**, 024319 (2012).

[64] B. A. Brown, Phys. Rev. Lett. **85**, 5300 (2000).

[65] K. Kaneko, M. Hasegawa, and T. Mizusaki, Phys. Rev. C **66**, 051306(R) (2002).

[66] N. Yoshinaga, K. Yanase, K. Higashiyama, and E. Teruya, Phys. Rev. C **98**, 044321 (2018).

[67] P. Van Isacker, Eur. Phys. J. Spec. Top. **229**, 2443 (2020).

[68] M. Bender, P.-H. Heenen, and P.-G. Reinhard, Rev. Mod. Phys. **75**, 121 (2003).

[69] D. Vretenar, A. V. Afanasjev, G. A. Lalazissis, and P. Ring, Phys. Rep. **409**, 101 (2005).

[70] T. Nikšić, D. Vretenar, and P. Ring, Prog. Part. Nucl. Phys. **66**, 519 (2011).

[71] P. Ring and P. Schuck, *The Nuclear Many-Body Problem* (Springer-Verlag, Berlin, 1980).

[72] T. Nikšić, D. Vretenar, and P. Ring, Phys. Rev. C **78**, 034318 (2008).

[73] T. Nikšić, N. Paar, D. Vretenar, and P. Ring, Comput. Phys. Commun. **185**, 1808 (2014).

[74] Y. Tian, Z. Y. Ma, and P. Ring, Phys. Lett. B **676**, 44 (2009).

[75] S. Teeti and A. V. Afanasjev, Phys. Rev. C **103**, 034310 (2021).

[76] T. Otsuka, A. Arima, F. Iachello, and I. Talmi, Phys. Lett. B **76**, 139 (1978).

[77] T. Otsuka, A. Arima, and F. Iachello, Nucl. Phys. A **309**, 1 (1978).

[78] J. N. Ginocchio and M. W. Kirson, Nucl. Phys. A **350**, 31 (1980).

[79] K. Nomura, N. Shimizu, and T. Otsuka, Phys. Rev. Lett. **101**, 142501 (2008).

[80] K. Nomura, N. Shimizu, and T. Otsuka, Phys. Rev. C **81**, 044307 (2010).

[81] S. Heinze, Computer Program ARBMODEL, University of Cologne (2008).

[82] G. A. Lalazissis, T. Nikšić, D. Vretenar, and P. Ring, Phys. Rev. C **71**, 024312 (2005).

[83] Brookhaven National Nuclear Data Center, http://www.nndc.bnl.gov

[84] T. Rzaca-Urban, K. Sieja, W. Urban, F. Nowacki, J. L. Durell, A. G. Smith, and I. Ahmad, Phys. Rev. C **79**, 024319 (2009).

[85] S. Chen, P. Doornenbal, A. Obertelli, T. R. Rodríguez, G. Authelet, H. Baba, D. Calvet, F. Château, A. Corsi, A. Delbart, J.-M. Gheller, A. Giganon, A. Gillibert, V. Lapoux, T. Motobayashi, M. Niikura, N. Paul, J.-Y. Roussé, H. Sakurai, C. Santamaria *et al.*, Phys. Rev. C **95**, 041302 (2017).

[86] C. Lizarazo, P.-A. Söderström, V. Werner, N. Pietralla, P. M. Walker, G. X. Dong, F. R. Xu, T. R. Rodríguez, F. Browne, P. Doornenbal, S. Nishimura, C. R. Niţă, A. Obertelli, T. Ando, T. Arici, G. Authelet, H. Baba, A. Blazhev, A. M. Bruce, D. Calvet *et al.*, Phys. Rev. Lett. **124**, 222501 (2020).

[87] R.-B. Gerst, A. Blazhev, N. Warr, J. N. Wilson, M. Lebois, N. Jovančević, D. Thisse, R. Canavan, M. Rudigier, D. Étasse, E. Adamska, P. Adsley, A. Algora, M. Babo, K. Belvedere, J. Benito, G. Benzoni, A. Boso, S. Bottoni, M. Bunce *et al.*, Phys. Rev. C **102**, 064323 (2020).

[88] M. Albers, N. Warr, K. Nomura, A. Blazhev, J. Jolie, D. Mücher, B. Bastin, C. Bauer, C. Bernards, L. Bettermann, V. Bildstein, J. Butterworth, M. Cappellazzo, J. Cederkäll, D. Cline, I. Darby, S. Das Gupta, J. M. Daugas, T. Davinson, H. De Witte *et al.*, Phys. Rev. Lett. **108**, 062701 (2012).

[89] P. D. Duval and B. R. Barrett, Phys. Lett. B **100**, 223 (1981).

[90] T. Kibédi and R. H. Spear, At. Data Nucl. Data Tables **80**, 35 (2002).

[91] E. Elhami, J. N. Orce, M. Scheck, S. Mukhopadhyay, S. N. Choudry, M. T. McEllistrem, S. W. Yates, C. Angell, M. Boswell, B. Fallin, C. R. Howell, A. Hutcheson, H. J. Karwowski, J. H. Kelley, Y. Parpottas, A. P. Tonchev, and W. Tornow, Phys. Rev. C **78**, 064303 (2008).

[92] M. Albers, K. Nomura, N. Warr, A. Blazhev, J. Jolie, D. Mücher, B. Bastin, C. Bauer, C. Bernards, L. Bettermann, V. Bildstein, J. Butterworth, M. Cappellazzo, J. Cederkäll, D. Cline, I. Darby, S. Das Gupta, J. Daugas, T. Davinson, H. De Witte *et al.*, Nucl. Phys. A **899**, 1 (2013).

[93] C. Kremer, S. Aslanidou, S. Bassauer, M. Hilcker, A. Krugmann, P. von Neumann-Cosel, T. Otsuka, N. Pietralla, V. Y. Ponomarev, N. Shimizu, M. Singer, G. Steinhilber, T. Togashi, Y. Tsunoda, V. Werner, and M. Zweidinger, Phys. Rev. Lett. **117**, 172503 (2016).

[94] F. Iachello and A. Arima, *The Interacting Boson Model* (Cambridge University Press, Cambridge, 1987).

[95] T. Thomas, K. Nomura, V. Werner, T. Ahn, N. Cooper, H. Duckwitz, M. Hinton, G. Ilie, J. Jolie, P. Petkov, and D. Radeck, Phys. Rev. C **88**, 044305 (2013).

[96] T. Togashi, Y. Tsunoda, T. Otsuka, and N. Shimizu, Phys. Rev. Lett. **117**, 172502 (2016).